QUANTIFICATION OF SECONDARY PHASES IN 6063 ALUMINIUM ALLOY

TAN SIN HOOI

A project report submitted in partial fulfilment of the requirements for the award of Bachelor of Engineering (Honours) Mechanical Engineering

Lee Kong Chian Faculty of Engineering and Science
Universiti Tunku Abdul Rahman

Sept 2021

DECLARATION

I hereby declare that this project report is based on my original work except for citations and quotations which have been duly acknowledged. I also declare that it has not been previously and concurrently submitted for any other degree or award at UTAR or other institutions.

Signature   :

Name   :   Tan Sin Hooi

ID No.   :   1606276

Date   :   4 August 2021

APPROVAL FOR SUBMISSION

I certify that this project report entitled **"QUANTIFICATION OF SECONDARY PHASES IN 6063 ALUMINIUM ALLOY"** was prepared by **TAN SIN HOOI** has met the required standard for submission in partial fulfilment of the requirements for the award of Bachelor of Engineering (Hons.) Mechanical Engineering at Universiti Tunku Abdul Rahman.

Approved by,

Signature	:	
Supervisor	:	Ts Dr. Chen Kah Pin
Date	:	24/9/2021

Signature	:	
Co-Supervisor	:	Ts Dr. Yeo Wei Hong
Date	:	24/9/2021

The copyright of this report belongs to the author under the terms of the copyright Act 1987 as qualified by Intellectual Property Policy of Universiti Tunku Abdul Rahman. Due acknowledgement shall always be made of the use of any material contained in, or derived from, this report.

ACKNOWLEDGEMENTS

First of all, I would like to express my gratitude to my research supervisor, Dr. Chen Kah Pin and co-supervisor, Dr. Yeo Wei Hong for the insightful advice, guidance and assist given throughout the research study.

Moreover, I would also like to express my gratitude to Tam Hui Mun's research work, without experimental result and data retrieved from Tam Hui Mun dissertation 'EFFECT OF HOMOGENIZATION TREATMENT ON THE 6063 ALUMINIUM ALLOY', I would not be able to conduct this research study in the first case.

Last but not least, I would like to thank Press Metal Berhad, an aluminium extrusion company where I conducted my industrial training. The invaluable knowledge acquired during the internship enables me to tackle this research study more easily.

ABSTRACT

The evaluation on AA6063 alloy's homogeneity by quantify secondary phases using appropriate techniques, investigate on the morphology and chemical composition of secondary phases present in AA6063 alloy, and the correlation between alloy's mechanical and microstructural properties are been conducted. Two types of secondary phases namely, $MgSi$ precipitates and $AlFeSi$ dispersoids has been quantified via various techniques. Optical microscopy (OM), scanning electron microscopy (SEM) with energy dispersive X-ray (EDX) identified these phases. Techniques to quantify secondary phases within AA6063 alloy rely on the difference in phase's morphology and chemical composition identified by material characterization techniques. $\alpha -$ and $\beta - AlFeSi$ phases were characterized and quantified based on the difference in dispersoid's aspect ratio, whereas β'' (Mg_5Si_6), β' ($Mg_{1.8}Si$) and β (Mg_2Si) precipitates were characterized based the difference in precipitate's diameter. Others microstructural properties such as crystallinity and crystallite size were also correlated with alloy's mechanical properties. The transformation of $\beta \rightarrow \alpha - AlFeSi$ dispersoids had increase in $Fe{:}Si$ atomic ratio and lower aspect ratio that quantifying $AlFeSi$ dispersoid based on dispersoid's aspect ratio. Correlation between alloy's mechanical properties and quantified secondary phase shows the sample alloy with higher elongation percentage consist of higher relative volume percentage of $\alpha - AlFeSi$. Indicates strong correlation between the alloy's ductility and the degree of $\beta \rightarrow \alpha - AlFeSi$ transformation within alloy. Moreover, the amount of $MgSi$ precipitates within alloy exhibit a good correlation with alloy's hardness, as findings shown that the higher the amount of $MgSi$ precipitates, the lower the alloy's hardness. However, no correlation can be made between alloy's mechanical properties and alloy's microstructural properties, namely crystallinity and crystallite size.

TABLE OF CONTENTS

CHAPTER

ix

LIST OF TABLES

LIST OF FIGURES

LIST OF SYMBOLS / ABBREVIATIONS

Al	Aluminium
Mg	Magnesium
Si	Silicon
Fe	Iron
Ti	Titanium
B	Boron
Mn	Manganese
Cu	Copper
Mg_2Si	Magnesium Silicate
β''	Beta double prime
β'	Beta prime
β	Beta
α	Alpha
π	Pi
AA	Aluminium alloy
DC	Direct Chill
VDC	Vertical Direct Chill
HDC	Horizontal Direct Chill
SSSS	Super Saturated Solid Solution
GP	Guinier-Preston
EDX	Energy dispersive X-ray
SEM	Scanning electron microscopy
TEM	Transmission electron microscopy
XRD	X-ray powder diffraction

LIST OF APPENDICES

CHAPTER 1

INTRODUCTION

1.1   General Introduction

Aluminium alloy extrusion is a comparatively inexpensive way of manufacturing complicated forms in long lengths with tight geometric tolerances. The process's versatility in terms of both the alloys that can be extruded and the forms that can be produced has resulted in the extensive use of aluminium extrusions in modern life (Reiso, 2004). Aluminium extrusions are the predominantly used alloys in the transportation and construction industries. It is used to make items such as window and door covers, building materials, roofing, and furniture (Bowden, 1984). According to Reiso (2004), extruded products accounted for one-third of all aluminium demand in Western Europe in 2001, with the bulk of extruded products employing 6000 series aluminium alloys, also known as $Al - Mg - Si$ alloys. Among the $Al - Mg - Si$ alloys, alloys such as AA6060 and AA6063 are the most commonly made. Because of the large volume generated, a productivity gain of just a few percent is a significant value, particularly in a market situation where the extruder is operating at maximum capacity (Røyset et al., 2019).

Over the years, industries have made significant efforts to optimise the production of lean $Al - Mg - Si$ alloys. This includes increased productivity as well as adequate mechanical properties. These factors allow aluminium alloy extruders to produce product at a low cost while maintaining desirable properties (Bowden, 1984). To achieve this goal, the alloy's extrudability and metallurgical properties have been optimised to produce high-productivity extrusion billets (Røyset et al., 2019).

As a result, industries implemented a heat treatment process known as homogenization, which provides high-quality billet for good extrusion products when compared to as-cast billet. This process reduces elemental microsegregation, grain boundary segregation, and the dissolution of low-melting eutectics, as well as the transformation of iron intermetallic, to produce a homogeneous microstructure that improves the extrudability and quality of as-cast billet (Sarafoglou et al., 2016; Uttarasak et al., 2019). Therefore, it is critical to identify evaluate billet's homogeneity in order to produce extrusion billets with maximum extrudability and desirable properties. According to numerous research studies, the evaluation of 6000 series

aluminium alloy's homogeneity is feasible by quantifying secondary phases present within the alloy identified via various characterization techniques as the present of secondary phases affects alloy's extrudability. Thus, quantification of secondary phase can evaluate billet's homogeneity.

Consequently, this research project employed several techniques implemented by researchers to quantify secondary phases within AA6063 alloys. The alloy's homogeneity was evaluated through qualitative examination of the billet's microstructure which characterized and quantify the secondary phases identified via various material characterization techniques.

1.2   Importance of the Study

In aluminium extrusion industry, the homogeneity of homogenized billet is one of the key factors that affects the productivity of extrusion process and the end product quality. Industry had demand for the evaluation on alloy's homogeneity to ensure the productivity.

Hence, quantification of secondary phases in homogenized alloy become very important as researchers mentioned that quantification of secondary phases can evaluate AA6063 alloy's homogeneity. As a result, it is important to use appropriate techniques to characterize and quantify the second phase present in AA6063 alloy. It was mentioned that the quantification of secondary phases, such as $AlFeSi$ dispersoids and $MgSi$ precipitates, can evaluate AA6063 alloy's homogeneity.

1.3   Problem Statement

According to Kelesoglu (2010), homogenization of aluminium extrusion billets facilitates extrusion and improves product quality. Therefore, it is critical to characterise quantitatively the homogeneity of AA6063 as-cast billets in order to produce extrusion billets that facilitates extrusion and improves product quality Sarafoglou et al. (2016).

From the studies of Kelesoglu (2010), Sun et al. (2014), Kuijpers et al. (2003), and Mrówka-Nowotnik (2010), the vary of homogenization parameter in term of soaking temperature and period or cooling rate applied to 6000 series aluminium alloy resulting different degree of $\beta \rightarrow \alpha - AlFeSi$ phase transformation with amount and sizes of $MgSi$ precipitates precipitated. These transformation or precipitation of

secondary phases affects alloy's extrudability, whereby quantify these secondary phases enable the evaluation of alloy's homogeneity.

Hence, this project assesses and compare techniques to characterize and quantify these secondary phases present in AA6063 to evaluate alloy's homogeneity. The quantification of secondary phases with different techniques will be assess and compare based on these secondary phases quantified via various characterization techniques with alloy's mechanical properties.

1.4   Aim and Objectives

The aim of this project is to evaluate alloy's homogeneity by characterizing and quantifying the secondary phases present in 6063 aluminium alloy using an appropriate technique. In order to fulfil the aim of this project, specific objectives needed to be achieved.

The objectives of this study are:

i.   To investigate the morphology and chemical composition of secondary phase present in AA6063 alloy.

ii.   To measure and quantify the present of secondary phases in AA6063 alloy via various material characterization techniques.

iii. To correlate the microstructural and mechanical properties of AA6063 alloy that undergone different homogenization treatment.

1.5   Scope and Limitation of the Study

The scope of the research project will focus on quantifying secondary phases that identified via various material characterization techniques through morphological identification and elemental analysis. The various material characterization techniques utilized in this paper to identify secondary phases within AA6063 that homogenized under different parameters includes optical microscopy (OM), scanning electron microscopy (SEM), energy dispersive X-ray (EDX), X-ray powder diffraction (XRD). In addition, this project will also assess and compare various material characterization techniques for identifying secondary phases based on the correlation between the alloy's mechanical properties examined by mechanical tests and secondary phases quantified by various characterization techniques. Mechanical tests included Vickers hardness test, tensile test, and compression test. Lastly, this study also consists of one

limitation, whereby in this study qualitative examination only conducted based on the limited experimental result and data retrieved from senior research work. Therefore, the result obtained might be suffering issue like low statistical power.

1.6 Contribution of the Study

In this research project, various techniques implemented by researchers to evaluate alloy's homogeneity through characterizing and quantifying secondary phases within homogenized 6000 series aluminium alloy had been assessed and compared, which may shed some light on the selection of suitable techniques for aluminium extrusion company to conduct qualitative examination on homogenized billet.

1.7 Outline of the Report

In this report, the importance of quantification of secondary phases in AA6063 alloys has been addressed in Chapter 1. Subsequently, literature review about the different in the morphology and chemical composition of secondary phases, and how do researchers employed various techniques to evaluate alloy's homogeneity had explored and discussed in Chapter 2. Furthermore, the explanation on experiment program conducted in this project and experimental data retrieved from Tam (2019) experimental work, along with the workflow for this research are stated in Chapter 3. Moreover, the results and discussions on the secondary phases quantified and characterized via various techniques and the alloy's mechanical properties under various homogenization parameters are critically analysed in Chapter 4. Lastly, conclusion of the study and recommendation for future works are described in Chapter 5.

CHAPTER 2

LITERATURE REVIEW

2.1   Introduction

In this chapter, the review of aluminium alloys and the factors of secondary phases in AA6063 alloys that affects the billet extrudability and product quality are been discussed. Besides that, various characterization techniques implemented by researchers to identify the effect of homogenization on the secondary phases in the heat treatable AA6063 alloys and the changes on AA6063 alloys mechanical properties as secondary phases changes due to homogenization treatment are been discovered. Moreover, various types of intermetallic phases and $Mg - Si$ precipitates within 6000 series aluminium alloy are been explored.hom

2.2   Aluminium alloys

Aluminium alloy is a non-ferrous metal that been widely applied in industry due to its advantageous physical and chemical properties such as light weight, strength, formability, and corrosion resistance, which such material is ideal for structural components (Triantafyllidis et al., 2015; Vargel, 2004). The high strength of aluminium alloy is achieved by adding alloying elements such as iron, silicon, magnesium, manganese, copper, and zinc into pure aluminium as strengthening agent due to the low strength of pure aluminium. In general, aluminium alloy improves strength through solution-hardening as alloying elements dissolved within $Al -$ matrix, or through precipitation hardening that forms precipitates within grains.

Furthermore, the strengthening mechanism of aluminium alloys also varies by the types of alloying elements added within aluminium, which heat treatable aluminium alloys strengthen through heat treatments that includes solution heat treatment, quenching, and precipitation, and age hardening, whereas non-heat treatable aluminium alloys gain strength by work hardening through mechanical deformation. According to aluminium alloy designation system, aluminium alloys that are heat-treatable are 2xxx, 6xxx, 7xxx, 8xxx series for wrought alloys and 2xx, 3xx, and 7xx series refers to casting alloys, where 4-digit classification and 3-digit classification are applied for wrought alloy composition designation and casting alloy composition designation, respectively (Davis, 2001).. Table 2.1 further illustrates the categorisation

of system based on the major alloying elements consist for each series of aluminium alloy as well as the strengthening mechanisms.

Table 2.1: Aluminium Alloy Designation System (Cobden and Banbury, 1994).

Wrought Aluminium Alloy		
Series	Major Alloying Element	Strengthening Mechanism
1 xxx	None (minimum 99.00% Aluminium, Al)	Work hardening
5 xxx	Magnesium, Mg	
3 xxx	Manganese, Mn	
4 xxx	Silicon, Si	
2 xxx	Copper, Cu	Heat treatment
6 xxx	Magnesium and Silicon, Mg + Si	
7 xxx	Zinc, Zn	
8 xxx	Others	
Casting Aluminium Alloy		
Series	Major Alloying Element	Heat treatable
1 xx.x	None (minimum 99.00% Aluminium, Al)	No
4 xx.x	Silicon, Si	
5 xx.x	Magnesium, Mg	
8 xx.x	Tin, Sn	
2 xx.x	Copper, Cu	Yes
3 xx.x	Silicon, Si (Copper, Cu and Magnesium, Mg are specified)	
7 xx.x	Zinc, Zn	

2.2.1   6063 aluminium alloy

6063 aluminium alloy is one of most popular alloys in 6000 series aluminium alloys that mainly consisting alloying elements: magnesium and silicon. The alloy is widely used in the manufacture of shaped aluminium profiles produced by extrusion due to its excellent extrudability (Isadare et al., 2015).

Moreover, 6063 aluminium alloy is also a heat treatable, light weight and non-ferrous metal alloy that able to provide high tensile strength and great ductility if

undergo proper heat treatment, whereby exceptional increases the alloy strength by precipitation hardening (Mrówka-Nowotnik, 2010). Proper heat treatment allows magnesium and silicon in 6063 aluminium alloys combine to form tiny magnesium silicide, Mg_2Si precipitates within Al-matrix which act as strengthening agent (Sheppard, 1999). The Mg_2Si precipitates enables 6063 aluminium alloy to attain high strength-to-weight ratio while provides good corrosion resistance, thereby being an attractive candidate to aerospace and automobile industries that demands ultralight materials for reduce in fuel consumption while increase the load carrying capacity (Isadare et al., 2015; Sun et al., 2014). In addition, Table 2.2 below illustrates the typical chemical composition of 6063 aluminium alloy.

Table 2.2: Chemical composition of 6063 aluminium alloys (Belov, Eskin and Aksenov, 2005).

Chemical Composition		Composition (%)
Magnesium, Mg		0.45 – 0.90
Silicon, Si		0.20 – 0.60
Iron, Fe		≤ 0.35
Other	Copper, Cu	≤ 0.10
	Manganese, Mn	≤ 0.10

2.3   Processing stage of a heat treatable aluminium alloy

According to aluminium alloy designation system, AA6063 is categorized as heat treatable alloy that mainly gain strength through heat treatment. The typical heat treatment processing stage for 6000 series heat treatable aluminium alloy aluminium alloys that undergo extrusion process are:

i.   Casting: The alloys are cast through direct chill (DC) casting, where vertical direct chill (VDC) casting technology is more commonly implemented by industries due to the capability to produce billet with high quantity, larger size and more favourable microstructure compared to horizontal direct chill (HDC) casting technology (Basic Metallurgy : 6000 Series Extrusion Alloys, 1997).

ii.   Homogenization: The alloys is heated from room temperature to around 575℃ for several hours, then cooldown at a controlled rate which modify the microstructure of as-casted billet, whereby improving the billet extrudability and enhancing the surface finishing and mechanical properties of final product (Sun et al., 2014; Basic Metallurgy : 6000 Series Extrusion Alloys, 1997).

iii.   Extrusion: The alloy is preheated to temperature around 440 to 490℃ then extruded through a die to create desired cross-sectional profile (Reiso, 2004).

iv.   Ageing: The extruded alloy profile is heated to around 185℃ for 5 hours to precipitate the strengthening particles (Basic Metallurgy : 6000 Series Extrusion Alloys, 1997).

Figure 2.1 illustrates the heat treatment of heat treatable alloy that undergoes extrusion process.
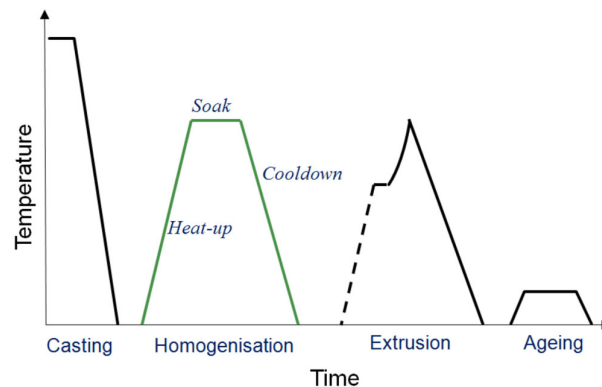
Figure 2.1: The typical processing stage of a heat treatable extrusion aluminium alloy (Rinderer, 2011).

2.3.1   Homogenization of as-cast aluminium alloy

Homogenization also known as solution treatment, is a heat treatment practice prior to extrusion process, which heated and soaked as-cast aluminium billet at an elevated temperature, and cooled down at a controlled rate (Sun et al., 2014).

The process enhances the extrudability of as-cast billet through modifies the microstructure of the billet so that during extrusion process, the required extrusion pressure is lowered, and therefore increases the production rate as extrusion speed increase. Besides, the modification in the microstructure of billet not only improved the extrudability of billet but also improves the surface finish and mechanical

properties of extruded profile as homogenization eliminate undesirable microstructure like as-cast eutectic morphology and compositional inhomogeneity which have deleterious effect to product quality (Kelesoglu, 2010; Sun et al., 2014).

Furthermore, there are also research mentioned that homogenization was practiced by industries to:

   i.   promotes the formation of dispersoids, which act as pins on grain borders, preventing recrystallization during extrusion (Mukhopadhyay, 2012; Rinderer, 2011).

  ii.   aids in the spheroidization of insoluble phases, which reduces stress concentration in the alloy, and thereby improves fracture toughness and surface finish (Uttarasak et al., 2019).

 iii.   dissolves the low-melting-point eutectic phases produced during casting, which melts during subsequent thermomechanical processes (Mukhopadhyay, 2012; Sun et al., 2014).

 iv.   eliminates microsegregation, resulting in uniform properties across secondary dendrite arm spacing (Mukhopadhyay, 2012; Rinderer, 2011).

2.4   Secondary phases in 6000 series aluminium alloy

There are two important secondary phases in 6000 series extrusion aluminium alloy that been account for attaining product with good mechanical properties and great surface quality, which are Mg_2Si phase and $AlFeSi$ phase. In order to attain high level of mechanical properties that these secondary phases in as-cast billet needed to be refined and modified through homogenization process.

According to Mrówka-Nowotnik (2010) and Bowden (1984), the morphology and amount of Mg_2Si secondary phase precipitated during the cooling stage of homogenization as well as the phase transformation of $\beta \rightarrow \alpha \ AlFeSi$ secondary phase during the soaking process of homogenization will strongly affects the end product quality.

2.4.1   AlFeSi phases

During the solidification of 6000 series aluminium alloys, intermetallic compounds such as $Al - Fe \ (Al_3Fe)$, $Al - Fe - Si \ (\beta - AlFeSi)$, and $Al - Fe - Mn - Si \ (\alpha - AlFeMnSi)$ phases are formed as eutectic reaction involving precipitation of Si and Fe containing phases occurs as Si content in Al alloys exceed the amount that is

necessary to form $Mg - Si$ precipitates (Belov, Eskin and Aksenov, 2005; Mrówka-Nowotnik, 2010). These insoluble intermetallic phases are also known as $AlFeSi$-based phases, which formed between the aluminium dendrites. According to Rosefort et al. (2011), variance of prevalent intermetallic phases in 6000 series were discovered by Kuijpers (2014) are shown in Table 2.3.

Table 2.3: The variance of the prevalent intermetallic phases in 6000 series (Kuijpers, 2014).

Phase	Structure	Stoichiometry
$\alpha_c(\alpha) - AlFeSi$	cubic	$Al_{12}Fe_3Si,$ $Al_{12-15}Fe_3Si_{1-2}$
		$Al_{12}(FeMn)_3Si,$ $Al_{15}(FeMn)_3Si_2$
		$Al_{12}Mn_3Si,$ $Al_{15}Mn_3Si_2,$ Al_9Mn_2Si
$\alpha_h(\alpha') - AlFeSi$	hexagonal	Al_8Fe_2Si
$\beta - AlFeSi$	monoclinic	$Al_{4.5}FeSi$

Besides that, Al_8Fe_2Si, Al_5FeSi, and $Al_8FeMg_3Si_6$ phases are also been reported by Belov, Eskin and Aksenov (2005), which these $AlFeSi$ phases are possibly formed in wrought 6000 series aluminium alloys. There are also $AlFeSi$ phases such as $(Fe, Mn, Cu)_3SiAl_{12}$, $(Fe, Mn)_3SiAl_{12}$, and $(Fe, Cu)_3SiAl_{12}$ that formed when there is presence of Cu and Mn in aluminium alloys.

2.4.2 Mg₂Si phases

Mg_2Si also known as magnesium silicide, is commonly used as a reinforcement phase to prepare aluminium-based metal matrix composites due to its excellent physical and mechanical properties. Mg_2Si has a low density ($1\,1.99 \times 10^3 \frac{kg}{m^3}$), high melting temperature (1085℃), high hardness ($4.5 \times 10^9 \frac{N}{m^2}$), high elastic modulus ($120GPa$) and low coefficient of thermal expansion ($7.5 \times 10^6 K^{-1}$), which make it commercially attractive (Triantafyllidis et al., 2015).

In 6000 series aluminium alloy, Mg and Si in solid solution in aluminium alloy will form $Mg - Si$ precipitates during the cooldown stage of homogenization process or during aging process. According to Triantafyllidis et al. (2015) and Mrówka-Nowotnik (2010), the precipitation sequence of metastable precursors of Mg_2Si in 6000 series aluminium alloys is:

$$SSSS \rightarrow atomic\ clusters \rightarrow GP - zones \rightarrow \beta'' \rightarrow \beta' \rightarrow \beta$$
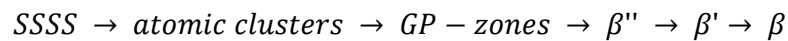
Firstly, the Mg and Si of super saturated solid solution will form atomic clusters around $\alpha - AlFeSi$ dispersoids, which acted as nucleation sites. Secondly, the atomic cluster grows into β'' (Mg_5Si_6) precipitates that is smallest with a rod-like shape, then as precipitation continues β'' becomes β' $(Mg_{1.8}Si)$, larger version of rod-shaped. Lastly, the β' will grow into β (Mg_2Si), the largest $Mg - Si$ precipitates that is cube-like in shape.

2.5   β→α-AlFeSi phase transformation

There are numerous authors had conducted research and study upon the $AlFeSi$ phase transformation from $\beta \rightarrow \alpha$ for as-cast 6000 series aluminium alloy as as-cast billet undergoes solution treatment. Based on these findings, this section collects relevant information that mentioned by researchers such as the importance of $\beta \rightarrow \alpha - AlFeSi$ phase transformation, and the characterization techniques implemented by researchers to identify type of $AlFeSi$ phase in aluminium alloy through examining identity, morphology, or chemical composition of $AlFeSi$ phase.

Triantafyllidis et al. (2015) studied about characterization of AA6060 alloy via micro-hardness Vickers test explained the importance of $\beta \rightarrow \alpha - AlFeSi$ phase transformation. They mentioned that although $AlFeSi$ phase do not contribute to the strength of alloy but, if the phases are not correctly processed, it will have a detrimental effect on the extrudability of aluminium alloy.

It is found that phase transformation affects the available level of Si-content in solid solution for precipitation of Mg-Si-precipitates in the final processing step of extrusions, and therefore the transformation is vital as it can greatly impact on the mechanical properties of final product. The reason why the precipitation of Mg-Si-precipitates is affected by $\beta \rightarrow \alpha - AlFeSi$ phase transformation as because the

amount of Si tied up in constituent Fe-rich phases formed during solidification and homogenization influences the level of Si content in solid solution.

Furthermore, Mrówka-Nowotnik (2010) that studied about the influence of chemical composition variation and heat treatment on microstructure and mechanical properties of 6000 series aluminium alloys agreed that precipitates of intermetallic phases consisting $Si, Fe \ and \ Mn$ play an importance role in mechanical properties.

Experimental results shown in Mrówka-Nowotnik (2010) stated the $AlFeSi$ phase in as-cast 6061 alloy that homogenized at a temperature of 575℃ for 72 hours had transformed. It is mentioned that such transformation increased the effectiveness of strengthening $\beta(Mg_2Si)$ phase as volume fraction of $\beta(Mg_2Si)$ precipitates are drastically decreased due to the formation of $AlFeSi$ phase during solidification of 6000 series aluminium alloys. Optical microscopy studies stated in the research shown that the as-cast microstructure which consisted of a mixture of $Al_3Fe, \alpha - AlFeSi \ and \ \beta - AlFeMnSi$ intermetallic phases distributed at grain boundaries (Figure 2.2a) was transformed from $\beta - AlFeSi$ phases into a more spheroidal $\alpha - Al(FeMn)Si$ phases after homogenization process (Figure 2.2b).
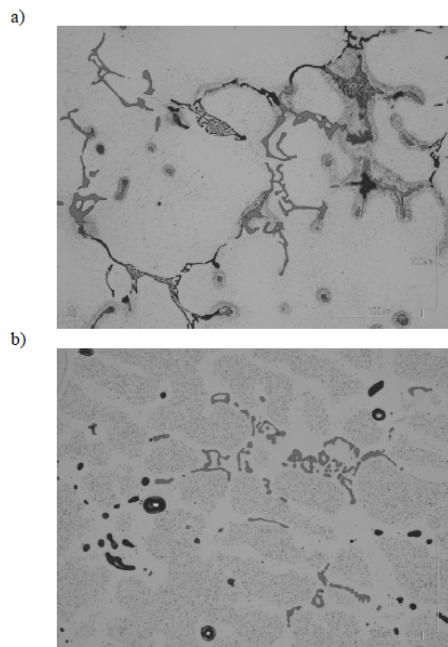
Figure 2.2: Microstructure of examined AA6061 alloy: a) as-cast state, b) after homogenization at 575℃/72h (Mrówka-Nowotnik, 2010).

According to the research of Kelesoglu (2010) which study on quantification of homogenizing treatment for $Al - Mg - Si$ alloy AA6063, authors had defined the homogenization level of an extrusion billets. Study stated in cast structure, the main insoluble intermetallic phase is $\beta - AlFeSi$, whereby such phase exhibits plate morphology that causes negative impact to the subsequent extrusion process and product quality. Therefore, the transforms $\beta \rightarrow \alpha \ AlFeSi$ defined the quality of homogenization practice. During homogenization treatment, $\beta - AlFeSi$ phase will break into pieces and transforms into $\alpha - AlFeSi$ phase, which relatively rounder and shorter.

Kelesoglu (2010) stated that using optical microscopy with differentiate technique mentioned by Kuijpers et al. (2003) that differentiating whether the $AlFeSi$ intermetallic phase is $\beta - AlFeSi$ or $\alpha - AlFeSi$ can be done. Authors differentiate $\beta -$ and $\alpha - AlFeSi$ phases through evaluating the length/width ratio of $AlFeSi$ intermetallic in the microstructure. Phases with ratio of $3:1$ or greater for length/breadth are expression of $\beta - AlFeSi$, whereas ratio lower than are considered as $\alpha - AlFeSi$ phases.

Moreover, this reasoning was implemented as the foundation for characterization technique employed by Kelesoglu (2010). Researcher investigated the microstructure of samples that machined from a commercial AA6063 extrusion billet that were homogenized at temperatures of 540, 560, or 580 °C for 2, 4, 6, 8, or 10 h via optical microscopy and tensile test. Inspection findings shown that in the cast structure, the area fraction of the $\beta - AlFeSi$ phase is over 65%, whereas well-homogenized sample, $\beta - AlFeSi$ area fraction decreases to values lower than 20%, while $\alpha - AlFeSi$ phase ratio increases to over 80% through comparison of the length/breadth ratio of $AlFeSi$ phases.

Optical micrographs also revealed as $\beta \rightarrow \alpha - AlFeSi$ phases transformation progresses, the discontinuity between aluminium dendrite cells diminishes, and cohesion increases. These are been proven as shown in Figure 2.3 and 2.4 which illustrates the morphology of $AlFeSi$ phases in the structure and the relative percentage of $\alpha -$ and $\beta - AlFeSi$ as a function of homogenization conditions, respectively.
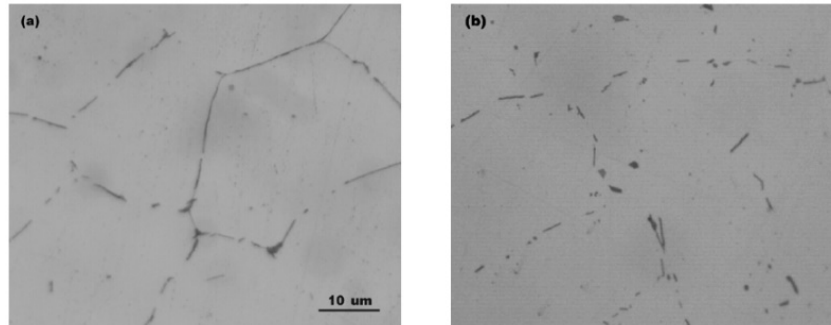
Figure 2.3: The morphology of AlFeSi phases in the structure, a) as-casted, b) homogenized at 560 °C for 6 h (Kelesoglu, 2010)
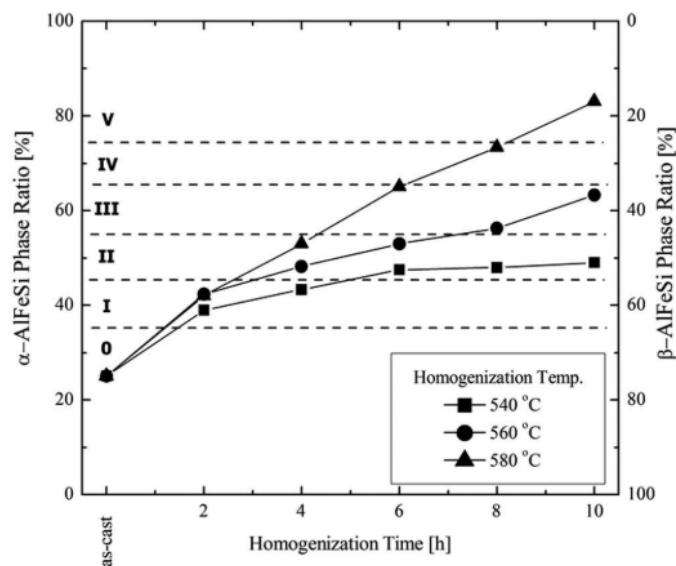
Figure 2.4: Relative percentage of α- and β-AlFeSi as a function of homogenization conditions (Kelesoglu, 2010)

Tensile tests carried out by Kelesoglu (2010) had justify the $\beta \rightarrow \alpha$ phase transformation during homogenization through evaluating the relationship between the deformation potential of samples and the homogenization level. Results obtained from tensile tests shown that as temperature and time of homogenization increase, the percentage of area fraction of $\alpha - AlFeSi$ in the structure increases whilst the elongation of samples rise from 1% to 24 %. Figure 2.5 illustrate the change in elongations of the samples at various temperatures and times.
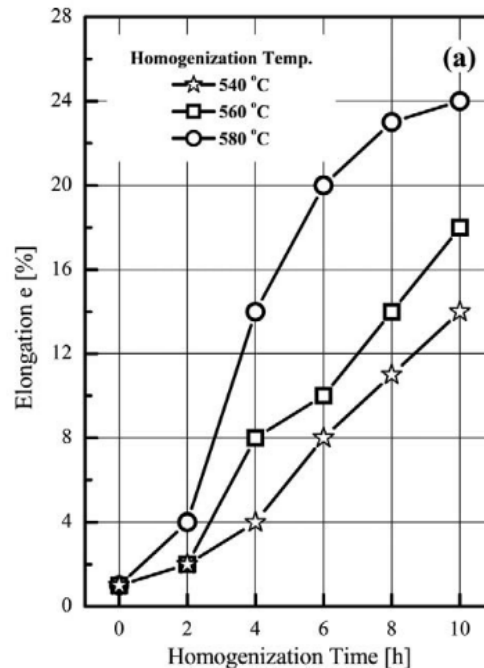
Figure 2.5: Elongation of the samples after homogenization at various temperatures and times (Kelesoglu, 2010)

Sun et al. (2014) studied about the effect of Mg_2Si phase on extrusion of AA6005 aluminium alloy had mentioned the changes in morphology of $\beta \rightarrow \alpha - AlFeSi$ phase. They also found that during soaking stage of homogenization treatment for 6000 aluminium alloys, the plate-like $\beta - AlFeSi$ intermetallic particles are transformed into more rounded α-$AlFeSi$ particles. Findings suggested that $AlFeSi$ intermetallic particles are the coarse particles distributed along grain boundaries in microstructures of specimens, which it was also mentioned that the transformation of these particles are not substantially influenced by the cooling rate of cooling practice during homogenization.

In addition, Rosefort et al. (2011) implemented a different but simple differentiation method for $\alpha -$ and $\beta - AlFeSi$ phases in wrought aluminium billets with the use of SEM and EDX. Authors stated that it is crucial to determine α and $\beta - AlFeSi$ phases due to the negative impact causes by $\beta - AlFeSi$ phases. However, authors claimed that determining these phases by considering the structure shape via microscopy is often impossible due to the low amount and small dimension of $AlFeSi$ phases appear in typical 6000 series aluminium alloys.

Therefore, authors claimed using EDX-measurement of element concentrations via the relation of Si and Fe content in the $AlFeSi$ phases, is a simple and fast method to differentiate $\alpha-$ and $\beta-AlFeSi$ phases. It is found that the typical Si/Fe ratio for $\alpha_c-AlFeSi$ are lower compares to $\beta-AlFeSi$ phases, which illustrated in Rosefort et al. (2011).
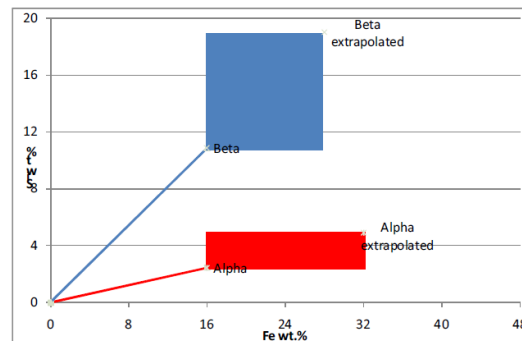
Figure 2.6: The typical Si/Fe ratio for α$_c$- and β-AlFeSi phases. (Rosefort et al., 2011)

Moreover, study also discovered different morphology of $AlFeSi$ phases. Authors declared that for aluminium alloy with low purity, $\alpha-AlFeSi$ phases will exhibit as curved crystals ("Chinese script") as shown in Figure 2.7, whereas $\beta-AlFeSi$ phases will exhibit as sharp and plate-like structure as shown in Figure 2.8.
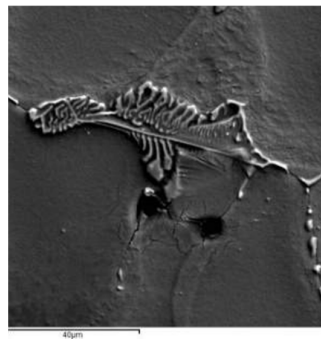
Figure 2.7: Curved structured α$_c$-AlFeSi phases shown in SEM images (Rosefort et al., 2011)
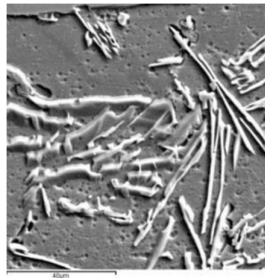
Figure 2.8: Plate-like β-AlFeSi phases shown in SEM images (Rosefort et al., 2011)

According to the research of Sweet et al. (2011) on the effect of Fe content on the Fe-containing intermetallic phases in as-casted AA6060 alloys, researchers had characterized Fe-containing intermetallic phases using scanning electron microscopy (SEM), optical microscopy, and transmission electron microscopy (TEM), thus identified the predominant $AlFeSi$ phase presented in as-cast and homogenized billet.

Sweet et al. (2011) observation on alloy with lower Fe levels via optical micrographs, authors discovered predominant phase appeared to be quite faceted with a needle-like morphology, which suggested that such predominant phase constituted as $\beta - Al_5FeSi$. On the other hands, predominant phase with Chinese-script morphology that found in alloy with higher Fe levels were suggested as $a_c - AlFeSi$ (Al_8Fe_2Si) phase. Figure 2.9 shows the optical micrographs which illustrate the typical morphology of intermetallic particles in the 6060 alloys containing (a) 0.1, (b) 0.2, (c) 0.3, and (d) 0.5 wt% Fe.
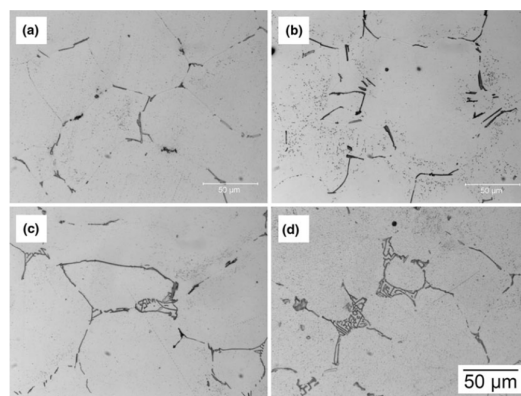
Figure 2.9: The optical micrographs which illustrate the typical morphology of intermetallic particles in as-cast AA6060 alloys containing (a) 0.1, (b) 0.2, (c) 0.3, and (d) 0.5 wt% Fe. (Sweet et al., 2011)

Moreover, scanning electronic microscopy studies stated in Sweet et al. (2011) revealed different features of $\beta-$ and $a_c-AlFeSi$ phase observed from optical micrographs that shown in Figure 2.10, 2.11 and 2.12. Under low magnification, faceted morphology of $\beta-Al_5FeSi$ is identified, whereas observation under high magnification, $\beta-Al_5FeSi$ phase displayed a lacy feature. Under low magnification, Chinese script $a_c-AlFeSi$ is identified, but observation of $a_c-AlFeSi$ under high magnification found to be quite featureless.
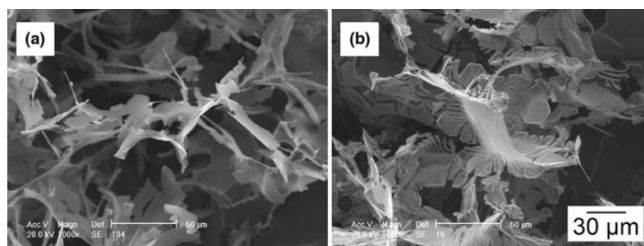
Figure 2.10: Morphology of $AlFeSi$ intermetallic phase revealed in low magnification SEM images. (a) β-Al₅FeSi phase in A6060 alloy consisting 0.1 wt% Fe and (b) ac -AlFeSi phase in A6060 alloy consisting 0.5 wt% Fe (Sweet et al., 2011).
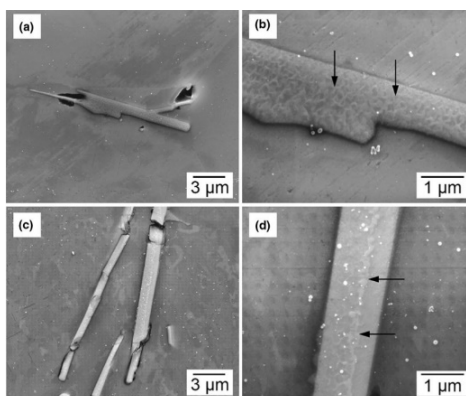
Figure 2.11: High magnification SEM images of faceted intermetallic phase in AA6060 alloys consisting (a) and (b) 0.1 wt% Fe 0.2, (c) and (d) 0.3 wt% Fe. Arrow indicated the lacy β-Al₅FeSi (Sweet et al., 2011).
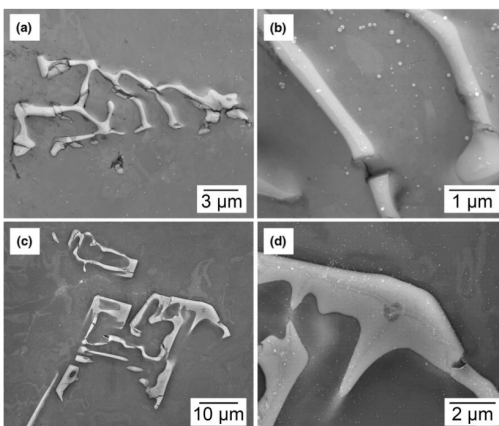
Figure 2.12: High magnification SEM images of Chinese-script intermetallic phase in AA6060 alloys consisting (a) and (b) 0.1 wt% Fe 0.2, (c) and (d) 0.3 wt% Fe. Arrow indicated the lacy β-Al₅FeSi (Sweet et al., 2011).

Besides, Sweet et al. (2011) also implement EDX-measurement to give an indication of $Fe:Si$ ratio in $AlFeSi$ phase, and thereby characterized $AlFeSi$ phases retrieved from TEM and SEM images. Sweet et al. (2011) mentioned that this enables the discrimination between $\beta-$ and $\alpha-$ phases. It was found that for Fe-containing phases with $Fe:Si$ atomic ratio of approximately 1 were considered as $\beta-Al_5FeSi$, whereas for phases with $Fe:Si$ atomic ratio that close to 2 are considered as $a_c-AlFeSi$ phases. Results shown that as Fe level in the alloy increased from 0.1 to 0.5 $wt\%$, the predominant faceted phases are replaced by phases with Chinese-script morphology and more phases with $Fe:Si$ ratio close to 2 were discovered as Fe contents increase.

In addition, Sweet et al. (2011) also had used TEM to examine the crystallography of the phases present. However, information about the distribution of phases is limited through TEM examination. Figure 2.13 shows the faceted $\beta-Al_5FeSi$ particle examined by EDX analysis was appeared to be sandwiched between two $\pi-Al_8FeMg_3Si_6$ phases. Figure 2.14 shows the images captured of $a_c-AlFeSi$ particles that examined by EDX analysis. The summary of types of $AlFeSi$ phase determined using different characterization techniques conducted by Sweet et al. (2011) research is shown in Table 2.4.
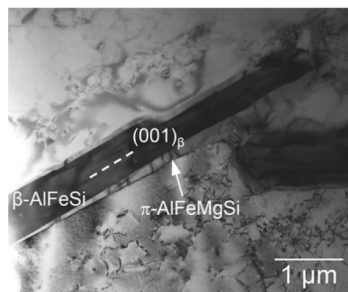
Figure 2.13: TEM image revealed β-Al_5FeSi and π-$Al_8(FeMg)_3Si_6$ phases in AA6060 alloy with Fe of 0.5 wt% (Sweet et al., 2011).

Figure 2.14: TEM image revealed an Al_cFe particle embedded within a_c-AlFeSi phase in the AA6060 alloy with Fe of 0.5 wt%(Sweet et al., 2011).

Table 2.4: Summary of Identified AlFeSi phases in AA6060 Alloy with Different Concentrations of Fe contents using Various Characterization Techniques (Sweet et al., 2011).

Fe (Wt pct)	Optical Observations	SEM (EBSD)	SEM (EDX)	TEM
0.1	Faceted phase (*i.e.*, elongated particles on grain boundaries)	β-Al_5FeSi	β Fe:Si ≈ 1	β-Al_5FeSi π-$Al_8FeMg_3Si_6$
0.2	Faceted phases (as above), plus some particles tending toward scriptlike	β-Al_5FeSi (major) $α_c$-AlFeSi (major) π-$Al_8FeMg_3Si_6$ Al3Fe (very small amount)	β Fe:Si ≈ 1 α Fe:Si ≈ 2	β-Al_5FeSi

0.3	Faceted phase: some Chinese-script phase	β-Al$_5$FeSi α_c-AlFeSi Al3Fe (minor)	β Fe:Si $\approx$ 1 α Fe:Si $\approx$ 2	β-Al$_5$FeSi π-Al$_8$FeMg$_3$Si$_6$
0.5	Chinese-script phase predominantly	α_c-AlFeSi (major) Al$_3$Fe (minor)	α Fe:Si $\approx$ 2	α_c-AlFeSi Al$_3$Fe (minor)

Moreover, Sweet et al. (2011) mentioned the formation of $a_c - Al_8Fe_2Si$ $particles$ in as-cast 6000 series aluminium alloys with high Fe contents discovered in this study was differ from the discrete $a_c - Al_{15}(Fe, Mn)_3Si_2$ phase particles shown in alloys with $Mn < 0.01\ wt\%$. It was stated that hexagonal form phase, $a_h - Al_8Fe_2Si$ was not discovered in Sweet et al. (2011) research due to the absence of Mn in experimental alloys. They indicated that such $a_c - Al(Fe, Mn)Si$ appeared in alloys with $Mn < 0.01\ wt\%$ will transform into $a_h - Al(Fe, Mn)Si$ after homogenization, which existed as a string of small particles ($1\ \mu m$) located along the positions of the original β particles.

Kumar, Grant and O'Reilly (2016) studied about the evolution of Fe bearing intermetallics during DC casting and homogenization of an $Al - Mg - Si$ aluminium alloy had determined the evolution of Fe-containing intermetallics phase during direct chill casting and homogenization of a grain-refined AA6063 alloy.

According to Kumar, Grant and O'Reilly (2016), research mentioned that the reduction in ductility by the planar geometry of $\beta - AlFeSi$ causes post-cast homogenization heat treatment is used commercially by industries as the treatment encourage the phase transformation of $\beta \rightarrow a$. Study suggested that $\alpha_c - Al(FeMn)Si$ is phases which had dendritic-like morphology and $\beta - AlFeSi$ is phase with plate-like morphology. Both phases that located at the grain boundaries are the dominant Fe-containing intermetallic phases in AA6063 alloys.

The characterized of $AlFeSi$ phases were identified via EDX analysis. Researchers characterized $AlFeSi$ phase with the Fe/Si ratio close to 2 as $a_c - AlFeSi$, and phase with the Fe/Si ratio of approximately 1 as $\beta - AlFeSi$. EDS-measurement shown that for homogenized billet, there will be higher fraction $a_c - AlFeSi$ compared to as-cast billet.

Besides, research also discovered the morphology of $AlFeSi$ phases. SEM images revealed that Fe-containing intermetallic phases with larger aspect ratio will exhibits script-like and needle-like morphology, whereas smaller aspect ratio particles had a rosette-like morphology. The script-like and rosette-like morphologies are attributed to $\alpha_c - Al(FeMn)Si$, whereas needle-like morphologies are attributed to $\beta - AlFeSi$. Figure 2.15 illustrates the morphology of the extracted particles captured via SEM.
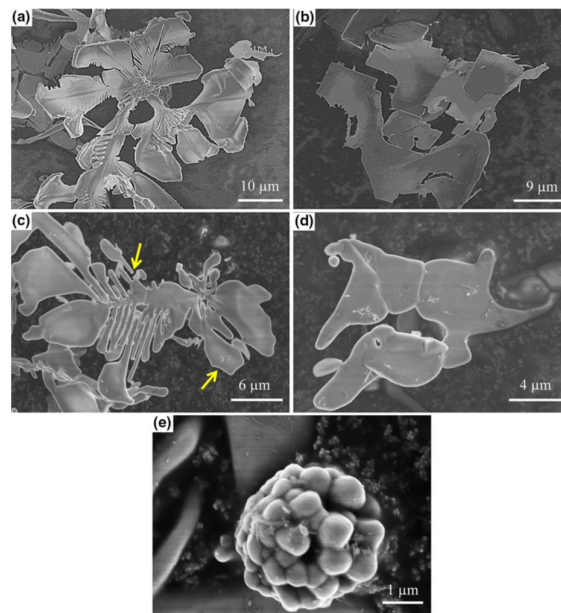
Figure 2.15: Scanning Electron Microscope images of extracted particles revealing (a) dendrite-like a_c-AlFeSi, (b) platelet-like β-AlFeSi, (c) partially dissolved dendrite-like a_c-AlFeSi, (d) disk-like a_c-AlFeSi and (e) rosette-like a_c-AlFeSi . Where (a through b) are from as-cast billet and (c through e) are from homogenized billet. (Kumar, Grant and O'Reilly, 2016)

Lastly, Kumar, Grant and O'Reilly (2016) suggested that the large needle-like or platelet-like $\beta - AlFeSi$ particles in as-cast billet transformed into discrete, fine, disk-like $\alpha_c - Al(FeMn)Si$ particles with an median length of $20\ \mu m$ after homogenization. The transformation occurs as the dissolve of $\beta - AlFeSi$ particles during homogenization fostered the nucleation and growth of $\alpha_c - Al(FeMn)Si$ through consuming the released Fe, Mn and Si by $\beta - AlFeSi$ particles.

According to the research of Kuijpers et al. (2003) about the model of $\beta - AlFeSi$ to $\alpha - Al(FeMn)Si$ transformation in Al-Mg-Si alloys stated that the transformation rate of plate-like $\beta - Al_5FeSi$ particles to multiple rounded $\alpha - Al_{12}(Fe,Mn)_3Si$ particles will determine the time required to homogenise the aluminium, as the transformation improves the processability of aluminium during extrusion. Negative impacts such as local crack initiation and induced surface defects are cause by the predominant $\beta - Al_5FeSi$ particles in as-cast billet, whereby explains why the transformed $\alpha - Al(FeMn)Si$ particles in homogenised billet are more preferable as it improves the extrudability of material and the surface quality of extruded profile.

Finite element approach was the model used in Kuijpers et al. (2003) to examine the transformation rate of $\beta - Al_5FeSi$ particles to $\alpha - Al_{12}(Fe,Mn)_3Si$ particles in an $Al-Mg-Si$ AA6005 alloy. Samples of AA 6005 alloys were homogenised at different temperatures of 540℃, 570℃ and 580℃ with times ranging from 10 minutes to 1 hour to discover the effect of homogenization temperature on the time required to transform $\beta - Al_5FeSi$ particles to $\alpha - Al_{12}(Fe,Mn)_3Si$ particles.

According to Kuijpers et al. (2003), finite element model simulates the $\beta \rightarrow \alpha$ phase transformation through the growth of $\alpha - particle$ on dissolving $\beta - plate$, which solely rely on the diffusion of Fe. This is because that transition rate of $\beta - Al_5FeSi$ to $\alpha - Al_{12}(Fe,Mn)_3Si$ is more influenced by Fe diffusion as the diffusion rate of Mn is lower compared to Fe. Therefore, research suggested that the effect of Mn absorption to the chemical composition of $\alpha - Al(FeMn)Si$ phases as $\beta - AlFeSi$ transform to $\alpha - Al(FeMn)Si$ was negligible.

In order to differentiate the type of $AlFeSi$ phases, researchers had implemented methodology that stated in Kuijpers et al., (2002). Based on this methodology, research had discovered the effect of Fe concentration in $Al -$matrix and the effect of homogenization temperature on the time required for $\beta -$ to $\alpha - Al(FeMn)Si$ transformation.

Kuijpers et al., (2002) methodology defined the parameters of finite element model, which classify $\beta -$ and $\alpha -$ phases. Kuijpers et al. (2002) discriminated $\beta - Al_5FeSi$ particles and $\alpha - Al_{12}(Fe,Mn)_3Si$ particles, according to the difference in stoichiometric ratio of the total concentration of Mn and Fe versus the concentration of Si via SEM with Electron Dispersive X-ray Spectography (EDX). It stated that

$AlFeSi$ phases with Fe/Si ratio of 1 are considered as $\beta - Al_5FeSi$, whereas phases with $(Fe + Mn)/Si$ ratio of 3 corresponds to $\alpha - Al_{12}(Fe, Mn)_3Si$.

Based on this categorization method stated by Kuijpers et al., (2002), that Kuijpers et al. (2003) used the relative fraction of $\alpha -$ particles with respect to the total amount of intermetallic as the equation to indicate the extrudability of material. Equation (2.1) shows that relative $\alpha -$ fraction, f_α, is established as:

$$f_\alpha = \frac{Volume\ (\alpha)}{Volume\ (\alpha) + Volume\ (\beta)} \tag{2.1}$$

Simulation result computed via finite element model shows that longer period of homogenization is required for $Al -$ matrix with lower Fe concentration to attain higher relative α -fraction. Figure 2.16 shows the relative $\alpha -$ fraction as a function of time under various initial Fe concentrations in the Al- matrix, which computed by finite elements model.
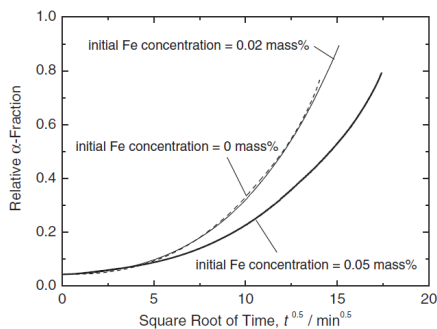
Figure 2.16: the relative α-fraction as a function of time under various initial Fe concentrations in the Al-matrix obtained from finite elements model (Kuijpers et al., 2003).

Moreover, their research shows that period of homogenization can be reduced while attained higher relative α-fraction through increase homogenization temperature, which illustrated in Figure 2.17.
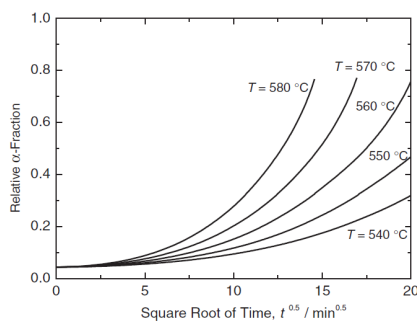
Figure 2.17: The relative α-fraction as a function of time under various homogenisation temperatures obtained from finite elements model (Kuijpers et al., 2003).

In addition, reason that why the location of the phase remains unchanged after phase transformation is described by researchers. Reason given was that α-particles nucleation occurs preferentially on the β/Al interface instead in Al-matrix as the activation energy required for nucleation of α particles on the β/Al interface is less compared to nucleation of α particles in Al-matrix.

Tang and Sritharan (1998) investigated the effect of Fe content and cooling rate on the crystallisation of $\beta - AlFeSi$ in AI_7Si casting alloy. The type of $AlFeSi$ phase was determined by examining the morphology of $AlFeSi$ phase via optical microscopy. Research outcomes shown that under normal casting condition, $\beta - AIFeSi$ ternary intermetallic phases (AI_5FeSi) is formed within the aluminium interdendritic as thin platelets. This $\beta - AIFeSi$ phase will be causing deleterious effects on the ductility and toughness on final products. However, dendritic $\alpha - AIFeSi$ (Al_8Fe_5Si) phase is less harmful to the mechanical properties of final product, and therefore the author recommend such preferable $\alpha - AIFeSi$ phase could be formed by adding alloying elements such as manganese (Mn) to the level of $Fe/Mn = 2:1$ to stabilize the formation of $\alpha - AIFeSi$ phase.

Based on their analysis, experimental results shown that only platelet morphology of $\beta - AIFeSi$ phase, which presented as long needle in metallographic section was found in all microstructure of as-cast Al_7Si alloy with three nominals Fe levels of $0.3, 0.6$ and $1.0\ wt\%$ were investigated at temperatures of 25 and $400°C$. Figure 2.18 and Figure 2.19 illustrates the optical micrograph of Al_7Si alloy casting under different temperature.
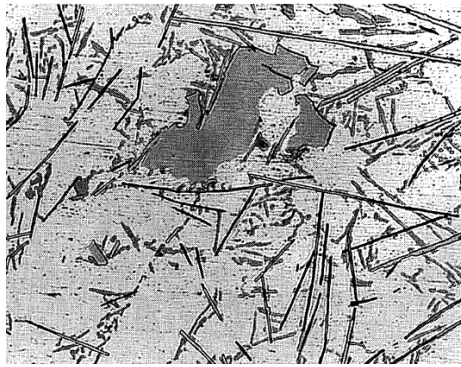
Figure 2.18: Optical micrograph of specimen with Si contents =6.72wt%, Fe contents =1.03wt% and mould temperature of 400°C (long needlelike phase is β-AlFeSi) (Tang and Sritharan, 1998)
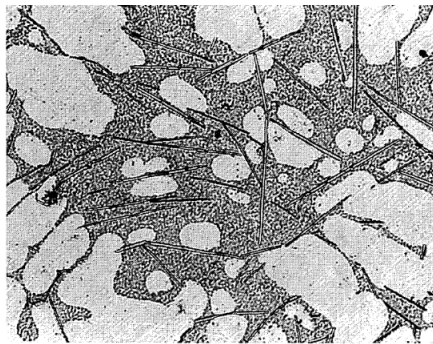
Figure 2.19: Optical micrograph of specimen with Si contents =6.66wt%, Fe contents =0.98wt% and mould temperature of 25°C (long needlelike phase is β-AlFeSi) (Tang and Sritharan, 1998)

Tang and Sritharan (1998) study also shown that decrease in cooling rate and increase in Fe content level encouraged the crystallisation of $\beta - AlFeSi$ and increases the size of β platelets. It was shown that platelet length increased by 200% when Fe content level rise from 0.6 to $1.0wt\%$. Figure 2.20 illustrates the plot of measured lengths of β platelets in metallographic sections against Fe content for given mould temperatures.
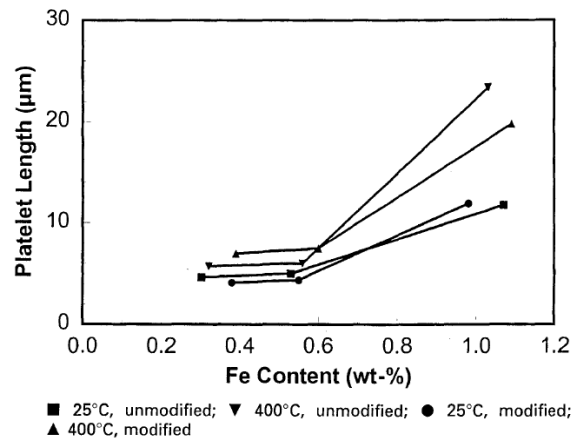
Figure 2.20: Plot of measured lengths of β platelets in metallographic sections against Fe content for given mould temperatures. (Tang and Sritharan, 1998)

Lastly, study also suggested that ductility of alloy will be improved by either increase the cooling rate or reduction in Fe content within the alloy as result shows β platelets length decreased due to reduce Fe content and lower cooling rate. In addition, study declared Si levels in alloy also will indirectly impact on the length of β platelet. It is discovered that alloy with high Si contents will have longer β platelets in comparison with alloys with low Si contents.

2.6   Precipitation of Mg₂Si phase

Precipitation of Mg_2Si phase in 6000 series aluminium alloy had been studied by researchers as this heat-treatable aluminium alloy mainly gain strength by precipitation hardening, which refers to precipitation of Mg_2Si precipitates. In this section, relevant information such as what is the ideal $Mg-Si$ precipitates for 6000 series aluminium alloy homogenized billet, different in identity and morphology for various types of $Mg-Si$ precipitates mentioned by various study and also the characterization techniques implemented by researchers.

According to Bowden (1984), author had mentioned the ideal Mg_2Si precipitates for homogenized billet. Research stated billet with the presence of large Mg_2Si particles could result crack initiation that appeared below the surface during extrusion, whereas billet that without these particles, cracking only occurs at the surface of extruded profile. It was mentioned that proper practice of homogenization was required to mitigate the presence of unfavourable large Mg_2Si particles during

extrusion, whereby cooling practice after homogenization determined the presence of Mg_2Si particles.

Based on the research, it was found that billet with low cooling rate after homogenization contains large and coarse Mg_2Si particle, which unable to dissolve during subsequent extrusion process. These undissolved particles may act as stress concentration locations, which result in void formation. Study suggested that proper cooling rate after homogenization is crucial as fast cooling rate can avoid Mg_2Si precipitation but billet that was rapid cooled could also face tearing defects due to the high strength of aluminium matrix contributed by $Mg + Si$ content in solid solution. These defects occur as the billet unable to resist the frictional forces in the extrusion die. Therefore, fine Mg_2Si precipitates in alloy are recommended as such precipitates are readily dissolved by the heat generated during extrusion.

According to Triantafyllidis et al. (2015), authors also had mentioned the Mg_2Si phase formed in homogenized billet. Study stated there were three categories of $Mg - Si$ precipitates. $\beta'' - Mg_5Si_6$, the rod-shaped smallest $Mg - Si$ and attributed mechanical properties when densely dispersed. $\beta' - Mg_{1.8}Si$, rod-shaped precipitate that relatively larger than β'' but it does not contribute strength to the alloy. $\beta - Mg2Si$, cube-like shaped precipitates that larger than β'' and β'. $\beta' - Mg_{1.8}Si$ is the prevalent $Mg - Si$ precipitates formed in homogenized billet, whereas metastable $\beta'' - Mg_5Si_6$ nanoscale precipitates was the prevalence intermediary phase formed in $Al-Mg-Si$ based alloy at during aging process (Røyset et al., 2019; Triantafyllidis et al., 2015).

Moreover, Rinderer (2011) stated that such β' precipitates with length between 1 to 2 μm in homogenized 6000 series aluminium alloys are preferred as the precipitates dissolved during the extrusion process, and thus product can attain good hardness during aging process. Findings also stated that $Mg - Si$ precipitates formed during aging process often discovered with length around $10 nm$, which smaller compared to precipitate in homogenized billet.

In addition, He et al. (2017) showed that AA6014 alloy sheet that solution-treated at 550°C for 1 minute was able to effectively dissolve Mg_2Si with diameter that less than 2 μm, whereas particles larger than 3 μm were unable to dissolve at such condition. This proven that under 550°C which similar as extrusion temperature, Mg_2Si particles smaller than 2 μm can be readily dissolve.

Moreover, Kumar, Grant and O'Reilly (2016) mentioned the location of Mg_2Si particles in grain refined $(Al - 5Ti - 1B)$ AA6063 alloy for as-cast and homogenized billet. It is discovered there are two location that Mg_2Si precipitated. In as-cast billet, Mg_2Si precipitates were found at grain boundary was close located with the needle-like $AlFeSi$ phase (Figure 2.21a), whereas Mg_2Si within Al −matrix was close located with the rosette-like $AlFeSi$ phase (Figure 2.21b). Experimental results mentioned in research stated that particles sizes of Mg_2Si in as-cast billet compared to homogenized billet were smaller. Based on the observation in as-cast and homogenized billets that the average equivalent size of Mg_2Si reported in study are $1.6 \pm 0.1\ \mu m$ and $2.9 \pm 0.2\ \mu m$, respectively.
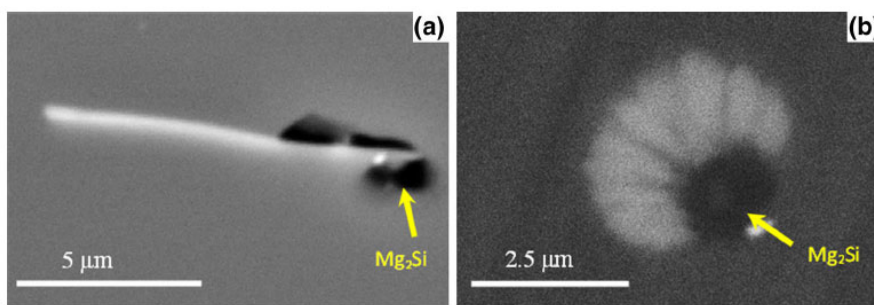
Figure 2.21: Images taken from as-cast AA6063 billet via SEM, which illustrated Mg2Si (dimmer particle) with (a) needle-like and (b) rosette-like AlFeSi phase (Kumar, Grant and O'Reilly, 2016).

Furthermore, the morphology of $\beta - Mg_2Si$ in $Al - Mg - Si$ based alloys were mentioned by Phongphisutthinan et al. (2013). Study stated that $\beta - Mg_2Si$ precipitates exhibit rod-like morphology with maximum length of $5\ \mu m$ after specimens were heated up to $723K$ and soaked for 2 hours, whereby it is discovered that the precipitation $\beta - Mg_2Si$ affects the hardness of alloy. It was suggested that $\beta - Mg2Si$ precipitates reduced the hardness of alloy as hardness of alloy was contributed by the solid solution of Mg and Si, whereby precipitation of $\beta - Mg2Si$ phase reduced the Si content in Al-matrix.

Besides, Asghar et al. (2020) had discovered the effect and size of $\beta'' - Mg_5Si_6$ precipitates and $\beta' - Mg_{1.8}Si$ precipitates. Study suggested that as the specimens were overaged that the needle-like β'' with average length of $20 \pm 2.9\ nm$ formed at peak aging condition had partially transformation into rod-shaped

β' precipitates with average length of $33 \pm 7.2 \; nm$ along, and thus causing reduction in the ductility of alloy.

Moreover, the following study conducted by Shafieizad et al. (2015) had described the morphological evolution of $Mg - Si \; precipitates$ in Al based alloy as the specimen was thermomechanically treated at homogenization temperature. Based on Shafieizad et al. (2015), effect of thermal disintegration and spheroidization on the changes in the morphology, size and distribution of Mg_2Si particles in $Al- Cu/Mg_2Si$ in-situ composite are discovered. Study mentioned that this effect brought by thermomechanical treatment eliminates undesirable primary and secondary reinforcement phases presented in as-cast specimen.

Scanning microscopy studies carried out by Shafieizad et al. (2015) had discovered the effect of thermal disintegration and spheroidization on secondary Mg_2Si particles and primary Mg_2Si particles. The two types of particles mentioned refers to coarse polygonal-shape primary Mg_2Si particles with relatively large mean circular diameter (15 μm) and secondary Mg_2Si phase with lamellar morphology that initially presented in as-cast microstructure.

The secondary Mg_2Si phase and primary Mg_2Si particles in as-cast specimens converted into dot-like shape and rounder shape through thermal disintegration and spheroidization mechanism as specimen compressed at 500℃. Reasoning mentioned by authors claimed that was because Mg_2Si particles tend to modify into more spherical shape due to the higher diffusion rate provided by sharp edges, which enables the dissolution of Mg and Si into Al-matrix and also such structure lowered required free surface energy of Mg_2Si particles. Figure 2.22 shows below is the schematic diagram of transformation as the as-cast secondary Mg_2Si precipitates undergo spheroidization when samples were compressed at 500℃.
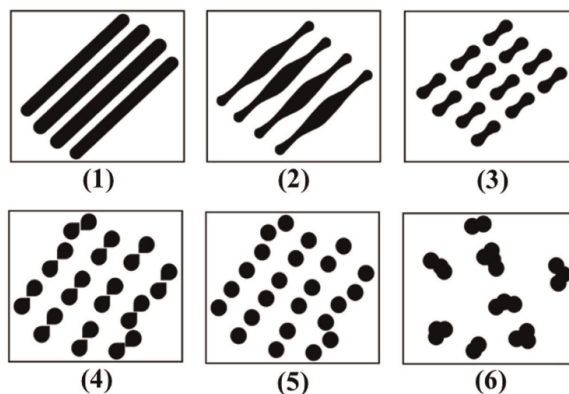
Figure 2.22: Schematic diagram of transformation as the as-cast secondary Mg₂Si precipitates undergo spheroidization when compressed under high temperature (Shafieizad et al., 2015).

Sun et al. (2014) claimed that it is important to optimize homogenization practice since the objectives of homogenization were to dissolve large Mg and Si-containing precipitates into $Al-$ matrix during the soaking procedure and to form Mg_2Si precipitates during the cooling procedure, both of which are beneficial for extrusion process. Findings shown that Mg_2Si precipitates had a significant impact on the billet's subsequent extrusion efficiency and the mechanical properties of final product. It was suggested that ideal Mg_2Si particles in microstructure are particles that often remain undissolved after preheating but readily dissolve upon deformation. As a result, modifying the cooling rate during homogenization necessitates a trade-off, whereby it was been reported that metastable $\beta' - Mg_2Si$ particles in alloys were beneficial for extrusion process as it improves extrudability.

Hardness test, hot compression test and quantitative analysis via optical microscopy were carried out on AA6005 alloy by Sun et al. (2014). Hardness test was implemented to evaluate the solution strengthening effect by Mg and Si in solid solution, and thereby determine the dissolution of Mg_2Si particles that affects the age hardenability of billet. Hot compression test was employed to examine the flow stress of billet under actual extrusion condition. Quantitative analysis via optical microscopy was to determine the size distribution of Mg_2Si particles.

Sun et al. (2014) showed that slow homogenization cooling rate will results increase in volume of smaller-sized Mg_2Si particles that spread within grains, whereby these coarsen particles were insolvable during extrusion. These particles can

significantly limit the extrusion speed, as it causes deleterious effect like incipient melting and surface defects. However, a fast-cooled billet with completely solutionized Mg and Si is also undesirable because the solid solution strengthening effect will induce a significant increase in flow stress during extrusion, causing the billet difficult to extrude. Figure 2.23 shows the optical micrographs illustrated Mg_2Si particles in homogenized AA 6005 specimens that soaked at 580 ℃ for 8 hours under different cooling rate.
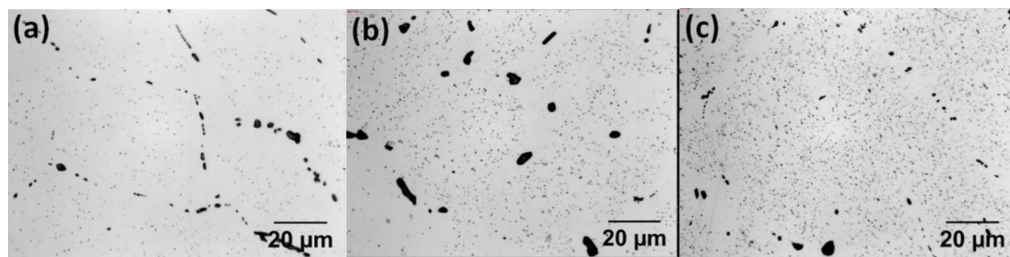
Figure 2.23: Optical micrographs of homogenized AA 6005 specimens with different cooling rate of (a) 500000 ℃/h (water quenching), (b) 3000 ℃/h (air cooling) and (c) 130 ℃/h (furnace cooling) (Sun et al., 2014)

Based on Sun et al. (2014) experimental results, research shown homogenized specimens undergo compression tests at billet preheating ($450\,℃$) and extrusion temperature ($500\,℃$ and $550\,℃$) with three different cooling rate, that specimens experienced highest cooling rate had the highest hardness, highest flow stress and decrease in Mg_2Si particles size, and vice versa. Besides, results shown that increase in temperature from 450 to 550℃ will reduces the flow stress on specimens.

In addition, Figure 2.24, 2.25, and 2.26 illustrate the changes in size distribution of Mg_2Si particles with different cooling rate, the hardness of AA 6005 specimens under different cooling rate, and effect of cooling rates on the flow stress of AA 6005 specimens under various temperatures are attached.
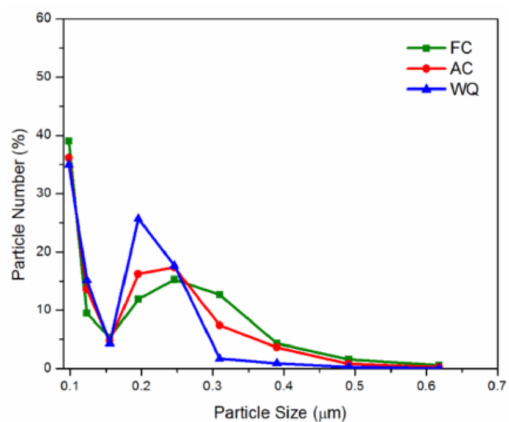
Figure 2.24: Size distribution of the Mg$_2$Si particles in AA 6005 alloy that cooled with different rates from soaking temperature (Sun et al., 2014).
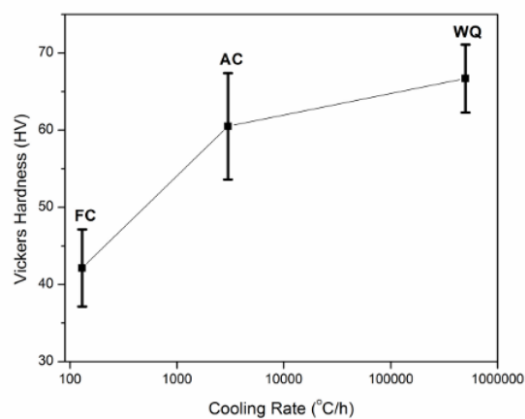
Figure 2.25: The hardness of AA 6005 specimens that soaked at 580 °C for 8 hours under various cooling rate (Sun et al., 2014).
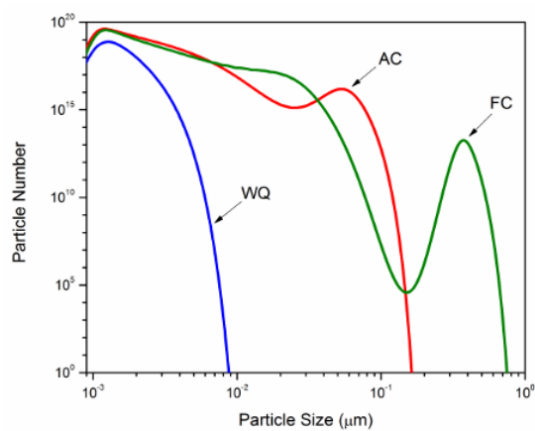
Figure 2.26: Effect of cooling rates on flow stress of AA 6005 specimens at various temperatures (Sun et al., 2014).

2.7   Summary

In summary, referring to literature reviewed there are mainly two types of secondary phases can be quantified for evaluation on billet's homogeneity, namely $AlFeSi$ dispersoids and $MgSi$ precipitates. $AlFeSi$ dispersoids enhanced alloy's ductility as higher degree of $\beta \rightarrow \alpha - AlFeSi$ phase transformation after homogenized. $MgSi$ precipitates reduce alloy's hardness and flow stress during extrusion as larger amount and sizes of $MgSi$ precipitates were precipitated with adequate cooling rate after homogenization process. Researchers mentioned that the degree of $\beta \rightarrow \alpha - AlFeSi$ phase transformation can be differentiated by its morphology that identified via OM or SEM, specifically through aspect ratio. Similarly, amount or sizes of $MgSi$ precipitates can be characterized via OM. Alternatively, literature reviewed also mentioned that $AlFeSi$ phase can be differentiated through elemental analysis via SEM with EDX due to major difference in $Fe:Si$ atomic ratio between β and $\alpha - AlFeSi$ phase. Consequently, quantifying these two secondary phases via various techniques mentioned by literature can identify the alloy's extrudability, thereby evaluate the alloy's homogeneity and also define the effectiveness of homogenization treatment.

CHAPTER 3

METHODOLOGY AND WORK PLAN

3.1   Introduction

This chapter is to outline the experiment program conducted in this project and experimental data retrieved from Tam (2019) experimental work, along with the workflow for this research. Materials prepared and experiments conducted by senior's research work along with experimental data retrieved from senior's research were explained thoroughly in this chapter. Experimental data retrieved from Tam (2019) were alloy's mechanical properties, alloy's microstructural images, alloy's crystalline phases and secondary phase's elemental composition. The alloy's mechanical properties were identified via tensile, compression and Vickers hardness test. The alloy's microstructural images were taken via optical microscopy (OM) and scanning electron microscopy (SEM). The alloy's crystalline phases were detected via XRD. The secondary phase's elemental composition, specifically $AlFeSi$ dispersoids were detected via EDX.

In present project, alloy's crystalline phases identified by XRD also used to estimate the crystallinity and crystallite size of alloy. Besides that, microstructural were utilized to investigate secondary phases present within alloys, namely $AlFeSi$ dispersoids and Mg_2Si precipitates. These images were then processed via image processing technique, which enable the characterization and quantification of secondary phases via image analysing software, ImageJ. The characterized and quantified secondary phases were then quantitatively analysed via data analysis and graphing software, Origin.

3.2   Materials

The materials used were as-cast AA6063 alloys produced by Press Metal Aluminium (PMA), one homogenized AA6063 alloy produced by Press Metal Sarawak (PMS) (Tam, 2019).

3.3   Work plan

In this section, the workplan for this research are described. Figure 3.1 illustrates the designed workplan to fulfil the aim and objectives for this project which includes

reviewing literature, examine alloy's mechanical properties that homogenized under different parameters through mechanical tests, quantify and identify the secondary phases identified via various material characterization techniques, and estimate the alloy's crystallinity and average crystallite sizes via XRD data.
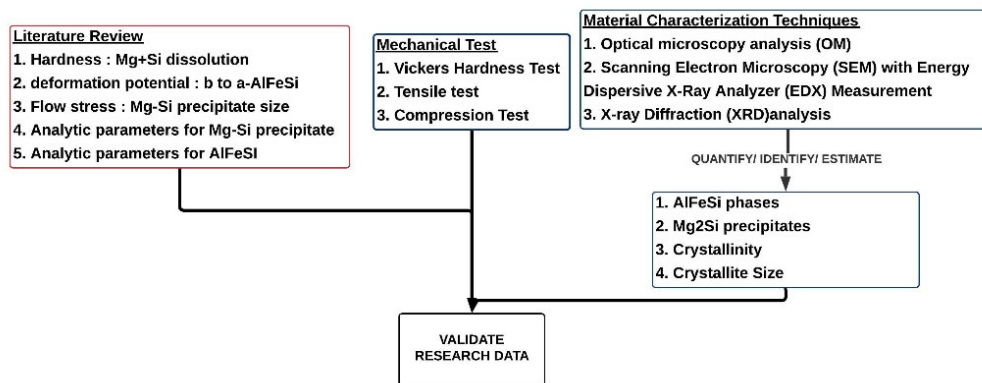
Figure 3.1: Work plan for attaining the aim and objectives of this project

3.4   Sample Preparation

Billets are machined into sample with respective dimensions, based on the dimension required by the experimental test and analysis conduct. Three machined as-casted sample were then undergone homogenization treatment under various soaking temperature, soaking period, and cooling rate. The parameters of homogenization treatment for the five specimens are stated in Table 3.1.

Table 3.1: The parameters of homogenization (Tam, 2019)

Specimen	Conditions	Soaking Temperature (°C)	Soaking Period (hours)	Cooling Rate
A	Homogenized, prepared in lab	520	2.0	Air Cooled
B		560	6.0	
C				
H	Homogenized, received from aluminium factory	580	3.5	Forced-Air Cooled
X	As-cast	-		Water quenched

3.5 Vickers hardness test

Digital Microhardness Tester, CV-400DM as shown in Figure 3.2 is the apparatus used to conduct Vickers hardness tests in accordance with ASTM standard E384, whereby a force of 100 gf was subjected onto the sample at a dwell time of 10 seconds (Tam, 2019). The hardness test result was used as evidence or data to verify or validate the statement made by researchers, whereby the hardness of specimens will decrease as more $MgSi$ precipitates formed in $Al-$martix.

Figure 3.2: Digital microhardness tester, CV-400DM

3.6 Tensile test

Universal tensile testing machine (UTM, Instron 5582Q4970) as shown in Figure 3.3 is the apparatus used to perform tensile test on specimens that had machined into dimension in accordance with ASTM B557 standard as shown in Figure 3.4 (Tam, 2019). The data extracted from the test was used to verify or validate the statement made by researchers, whereby the degree of $\beta \rightarrow \alpha - AlFeSi$ phases transformation will improve the ductility of billet.

Figure 3.3: Universal Tensile Testing Machine (Instron 5582Q4970)

,,1,
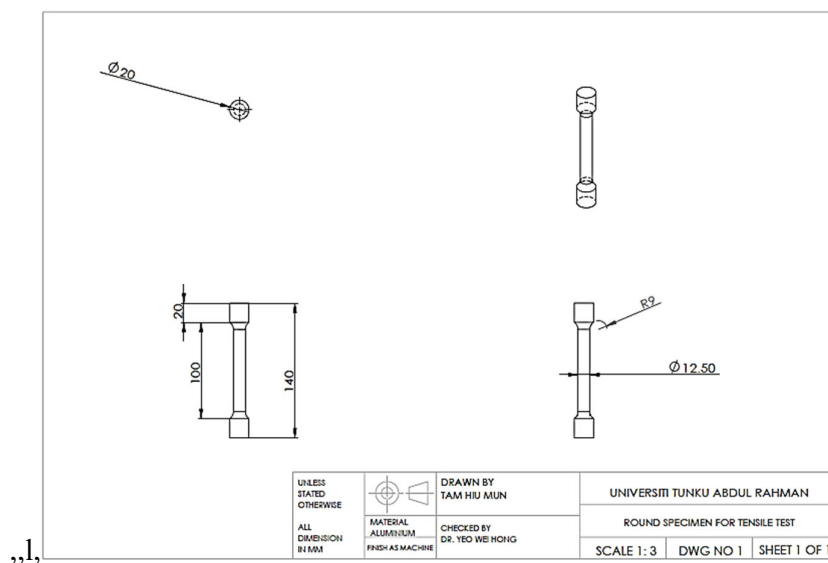
Figure 3.4: Engineering drawing of the samples (Tam, 2019)

3.7 Compressive Test

Universal tensile testing machine (UTM, Instron 5582Q4970) as shown in Figure 3.5 is the apparatus used to conduct compressive test, whereby $2\ kN$ of compressive force was applied at the beginning, which then end once the compressive force reaches $90\ kN$ (Tam, 2019). This experimental data was used to verify the statement made by researchers, whereby precipitation of $Mg - Si$ precipitates will reduce the billet's flow stress.

Figure 3.5: Experimental Setup of Compressive Test (Tam, 2019)

3.8   X-ray Diffraction (XRD) analysis

X-ray diffractometer (Shidmazu XRD-6000) as shown in Figure 3.6 was the apparatus used to conduct X-ray diffraction (XRD) analysis. This experimental data was used to identify crystalline phase using HighScore Plus and to identify whether there were changes in crystalline size or degree of crystallinity after homogenization via Scherrer equation and XRD deconvolution method, respectively.

Figure 3.6: X-ray diffractometer (Shidmazu XRD-6000)

3.8.1   Phase Identification

In this section, XRD data implemented for phase identification procedures are described. The procedures are described as follow:

1. Open the XRD data file via Highscore Plus
2. Go to "Analysis", then "Search and Match", and search for the compound that most fit with the XRD pattern detected. The compound that highly matched with the XRD pattern will has the highest score and listed at the top of selected candidate list as shown in Figure 3.7.

Figure 3.7: Compound that most fit the XRD pattern detected

3. Click on the reference code that highly matched with XRD pattern to retrieve the compound's JCPDS card.
4. Save the JCPDS card.

3.8.2 Crystallinity Analysis

In this section, the procedures to calculate crystallinity from XRD data via Origin are described. The procedures are described as follow:

1. Input data such as peak position and intensity from XRD data into Origin, then generate line graph as shown in Figure 3.8.
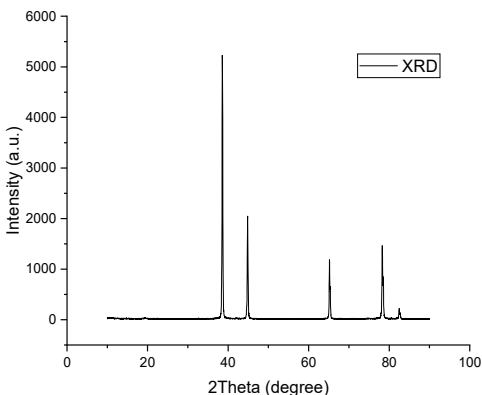
Figure 3.8: Sample generated line graph

2. Go to "Analysis", then go to "Peaks and Baseline", then go to "Peak Analyzer", then select "Open Dialog", which then a "Peak Analyzer" tab will pop up.
3. Click "Next" thrice, then select "Add" to select the peak position of XRD pattern matched with JCPDS card as shown in Figure 3.9.
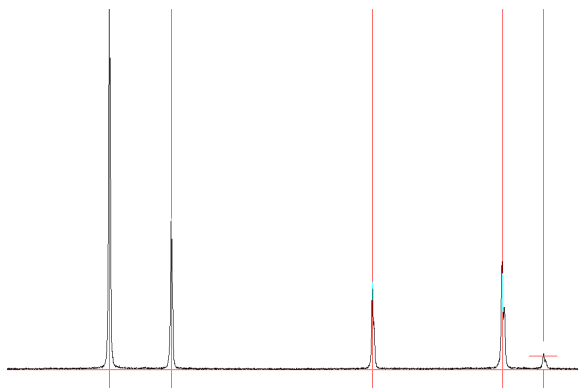
Figure 3.9: Selected peak position

4. After selected all peak position, click "Done", then select "Positive" under "Direction" section, then click "Next", then click "Finish". The software then generates a report sheet that consist of the area of all selected crystalline peaks as shown in Figure 3.10.

Index	Area
Integral Result of "Intensity"	Integral Result of "Intensity"
1	1335.56
2	523.76
3	338.48
4	544.2
5	90.22

Figure 3.10: Area of all selected crystalline peaks

5. Repeat Step 2 procedure on the previous generated line graph.
6. Click "Next" thrice, then select "Positive" under "Direction" section, then click "Next", then untick "All Peaks", then enter "1" for "Number of Ranges to Integrate" and select "Adjust on Preview Graph".
7. Select all peak within XRD pattern as shown in Figure 3.11, then retrieve the total area of all peaks from "Data Display" as shown in Figure 3.12.
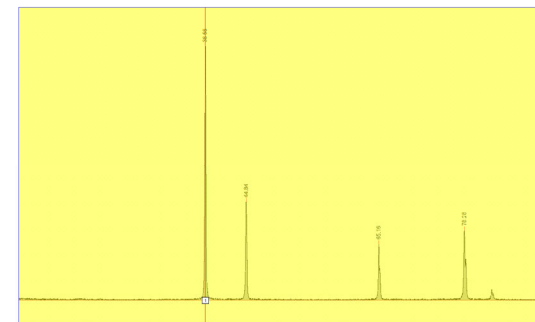
Figure 3.11: Select all peaks
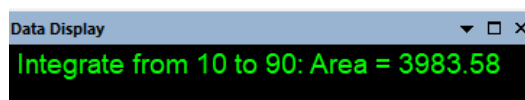
Figure 3.12: Total area of all peaks shown in "Data Display"

8. Lastly, based on the total area of crystalline peaks and the total area of all peaks obtained from XRD data that crystallinity can be calculated using following equation:

$$Crystallinity = \frac{Total\ Area\ of\ crystalline\ peaks}{Total\ Area\ of\ all\ peaks} \times 100\%$$

3.8.3 Crystallite Size Analysis

In this section, procedures to calculate average crystallite size from XRD data via Origin are described. The procedures are described as follow:

1. Similar procedure as Step 1 and 2 stated in Chapter 3.8.2.
2. Go to "Analysis", then "Peaks and Baseline", then "Multiple Peak Fit", then select "Open Dialog". A tab "Multiple Peak Fit: nlfitpeaks" will pop up.
3. Click "OK", then select all crystalline peaks similar as Figure 3.9.
4. Click "OpenNLFit", then click "Fit until it converged" icon, then click "Done". A report sheet that consists of FWHM and peak position of selected crystalline peaks is generated.
5. Calculate value of $In(\frac{1}{cos\theta})$ and $In(\beta)$ based on the β, FWHM and θ, peak position from the report sheet generated.
6. Input the calculated value of $In(\frac{1}{cos\theta})$ and $In(\beta)$ into Origin, then generate scatter diagram as shown in Figure 3.13.
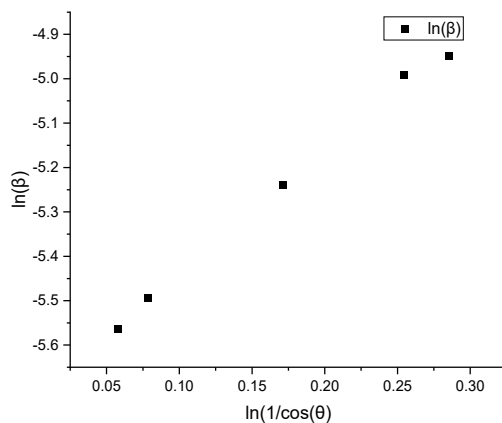
Figure 3.13: Sample scatter diagram of $In(\frac{1}{cos\theta})$ vs $In(\beta)$

7. Go to "Analysis", then go to "Fitting, then go to "Linear Fit", then select "Open Dialog" and click "OK". A regression line is generated in the graph as shown in Figure 3.14.
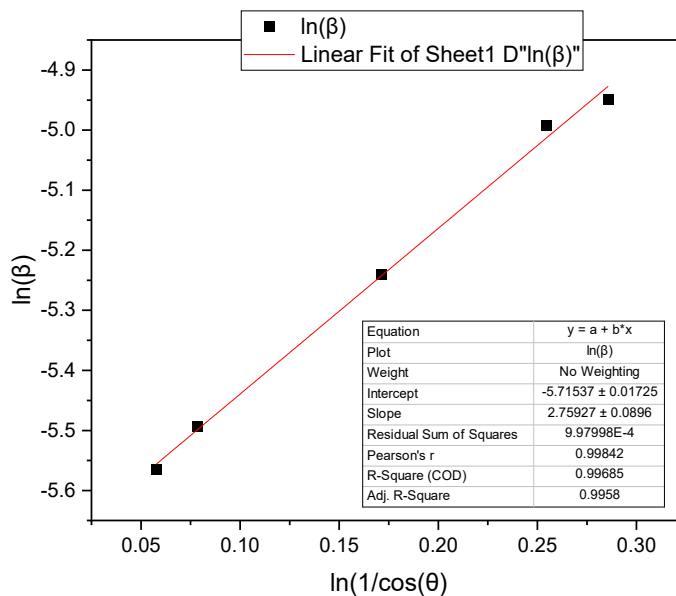
Figure 3.14: Linear Regression Model of $In(\frac{1}{cos\theta})$ vs $In(\beta)$

8. Lastly, based on the value of y-intercept provided from the table within Figure 3.14 that the average crystallite size can be calculated via following equation:

$$average\ crystallite\ size = \frac{K\lambda}{e^{\text{y}-\text{intercept}}}$$

K(Scherrer constant)$= 0.9; \lambda$(wavelength of x-ray sources)$= 0.15406nm$

3.9 Metallographic Examination

3.9.1 Optical microscopy (OM) analysis

Optical microscope (OM, Olympus BX61) as shown in Figure 3.15 was the apparatus used to conduct optical microscopy on etched specimen. Optical microscopy can examine the morphology of secondary phases presented in specimen. The types of secondary phases in alloy are differentiate through phase's morphology and location identified from microstructural images taken via OM. The microstructural images taken via OM was used to identify the presence of $Mg - Si$ precipitate and $AlFeSi$ disperiods in AA6063 that homogenized under different parameters.

Figure 3.15: Optical microscope (OM, Olympus BX61)

3.9.2 Scanning Electron Microscopy (SEM) analysis with Energy Dispersive X-Ray Analyzer (EDX) Measurement

Scanning electron microscope (SEM, Hitachi S-3400N) as shown in Figure 3.16 was the apparatus used to conduct scanning electron microscopy on etched specimen. Scanning electron microscopy identify the types of secondary phases presented in specimen through phase's morphology and location. In addition, energy dispersive spectrometer (EDX) can also characterize secondary phases in specimen through difference in chemical composition of secondary phases. The microstructural images

taken via SEM and elemental identification provided by EDX were used to differentiate the types of *AlFeSi* dispersoids within the alloy.

Figure 3.16: Scanning electron microscope (SEM, Hitachi S-3400N)

3.9.3   Image Analysis

In this section, image processing techniques were implemented in ImageJ, image analysing software are described. The procedures are described as follow:

5. Open the microscopy image via ImageJ
6. Use line feature in ImageJ to draw line on top of the scale bar provided in microscopy images, which located at the bottom left corner of the image as shown in Figure 3.17.
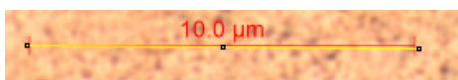
Figure 3.17: Scale Bar in OM image

7. Go to analyse, modify the value for distance and unit in accordance with the scale bar value as shown in Figure 3.18.
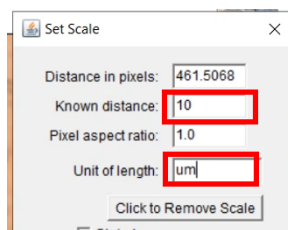
Figure 3.18: Adjust Scale Setting

8. Eliminate unwanted phases and scratches via painting tool as shown in Figure 3.19.
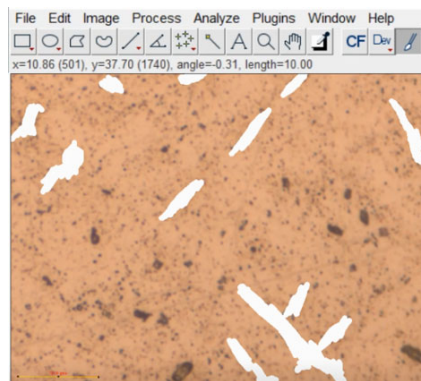
Figure 3.19: Sample result of eliminating unwanted phases and scratches from OM images

9. Change the OM or SEM image to grey scale image by go to manual, image type, choose 8, 16 or 32 bits. Figure 3.20 shows a sample of grey scale OM image.
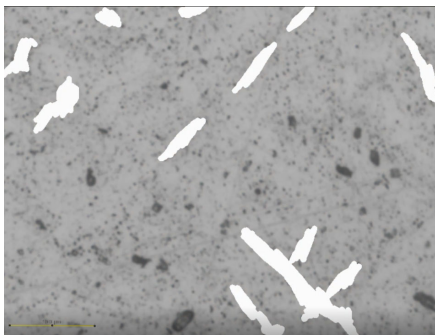
Figure 3.20: Sample of grey scale OM images

10. Go to image, adjust, then threshold to filter the image by colour. In this step, secondary phases will be highlighted which enable the software to measure the phases automatically.

11. Go to analyse, analyse particles then tick both "display results" and "clear result" to show the image and the measured value.

12. An image will be generated which show the measured particles along with dimensionless shape factors such as aspect ratio and max ferret diameter of the measured phases. Figure 3.21 illustrates a sample result described by step 7.
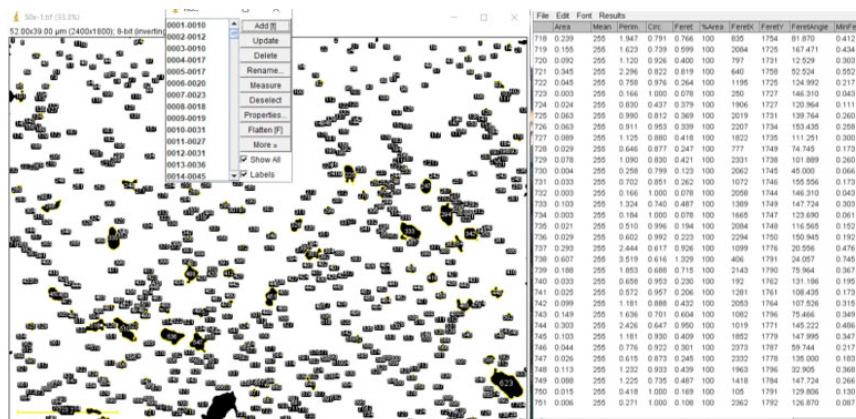
Figure 3.21: Sample result obtained from ImageJ for secondary phases measurement

13. Finally, referring to measurement retrieved from phases analysed that scientific graphing and data analysis can be conducted via data analysis software, Origin. For instances, generating histogram for the size distribution of secondary phases or scatter diagram for the correlation between secondary phases and alloy's mechanical property.

3.10 Characterization Parameters for AlFeSi phases

Based on research findings mentioned by various articles, the analytical parameters for $AlFeSi$ phases via optical analysis are defined. Table 3.1 illustrates the optical characterization parameters implemented in this study with the references retrieved from various research articles to determine the difference between $\alpha-$ and $\beta-$ $AlFeSi$ phases. Furthermore, according to Mrówka-Nowotnik (2010), Sun et al. (2014), and Kumar, Grant and O'Reilly (2016) that both $\alpha-$ and $\beta-AlFeSi$ phases exist at the grain boundaries in $Al-$matrix. In addition, equation 2.1 retrieved from Kuijpers et al. (2003) will be used to indicate the relative volume percentage of $\alpha-$ and $\beta-AlFeSi$ identified from samples.

Table 3.2: Characterization Parameters for AlFeSi phases

Aspect Ratio		
Types	Parameters	References
$\beta - AlFeSi$	Phases with ratio of 3:1 or greater	(Kelesoglu, 2010) (Kuijpers et al., 2003)
$\alpha - AlFeSi$	Phases with ratio lower than 3:1	

3.11 Characterization Parameters for Mg-Si precipitates

Based on research findings mentioned by various articles, the analytical parameters for $Mg - Si$ precipitates via optical analysis are defined. Table 3.2 illustrates the optical characterization parameters implemented in this study with the references retrieved from various research articles to determine the difference categories of Mg_2Si precipitates. In addition, according to Mrówka-Nowotnik (2010) and Kumar, Grant and O'Reilly (2016) that $Mg - Si$ precipitates are usually found within the grain in $Al -$matrix.

Table 3.3: Characterization Parameters for Mg-Si precipitates

Max Diameter (D)		
Types	Parameters	References
$\beta'' - Mg_5Si_6$	$D < 0.2\ \mu m$	(Asghar et al., 2020) (Rinderer, 2011) (Røyset et al., 2019) (Sun et al., 2014)
$\beta' - Mg_{1.8}Si$	$0.2\ \mu m \leq D \leq 5\ \mu m$	(Rinderer, 2011) (Phongphisutthinan et al., 2013)
$\beta - Mg_2Si$	$D > 5\ \mu m$	(Phongphisutthinan et al., 2013) (Shafieizad et al., 2015)

3.12 Elemental Analysis for AlFeSi phases

Based on research findings mentioned by various articles, the analytical parameters for $AlFeSi$ phases via elemental analysis are defined. Table 3.3 illustrates the elemental characterization parameters implemented in this study with the references

retrieved from various research articles to determine the difference between $\alpha-$ and $\beta-AlFeSi$ phases.

Table 3.4: Elemental Characterization Parameters for AlFeSi phases

$Fe:Si$ atomic ratio (R)		
Types	Parameters	References
$\beta-AlFeSi$	$R \leq 1.5$	(Sweet et al., 2011)
$\alpha-AlFeSi$	$3 \geq R > 1.5$	(Rosefort et al., 2011) (Kumar, Grant and O'Reilly, 2016) (Kuijpers et al., 2002)

3.13   Summary

In summary, the project will be carried out in accordance with the methodology and work plan stated in this chapter. The methodology of the project was designed in order to achieve the aims and objectives of the project. The crystalline phase of alloy is identified via Highscore Plus and the crystallinity with the average crystalline size are calculated using Origin. The quantification of secondary phases is carried out based on the characterization parameters to differentiate the types of secondary phases identified via various material characterization techniques. Alloy's microstructural properties and mechanical properties were identified using senior's experimental work and data.

CHAPTER 4

RESULTS AND DISCUSSION

4.1   Introduction

In this chapter, discussion was made based on the experimental result and analysis conducted and retrieved from senior's research work. The discussion includes the correlation between sample's mechanical properties and the homogenization process parameters subjected by sample, the correlation between the quantified secondary phases and the homogenization process parameters subjected by sample, and the correlation between sample's microstructural properties and sample's mechanical properties.

This chapter assess and compare the various technique implemented by researchers for quantifying secondary phases to evaluate the billet's homogeneity.

4.2   XRD analysis

Figure 4.1 shows the phase constitutions for samples and the reference XRD pattern of aluminium peaks. Analysed result shown that all samples' XRD patterns match precisely with the standard data (JCPDS card no. 03-065-2869), indicating the existence of aluminium peaks. However, existence of $AlFeSi$ dispersoids and $MgSi$ precipitates were not detected due to the limited detection capability of XRD equipment employed by Tam (2019).
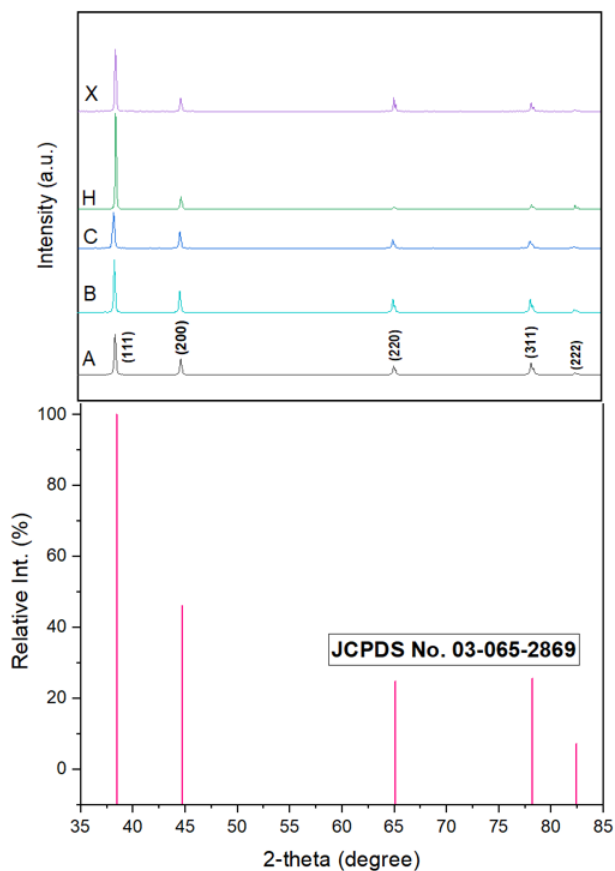
Figure 4.1: The phase constitutions of A, B, C, H, X as characterized by XRD

Moreover, crystallite size and crystallinity analysis also been conducted to evaluate the relationship between crystallite size or crystallinity with the sample hardness. Table 4.1 shows the crystallite size calculated using Scherrer equation and the crystallinity calculated using XRD deconvolution method based on XRD data.

Table 4.1: Crystallite size and crystallinity of samples

Sample	Crystallite Size (nm)	Degree of crystallinity (%)
A	42.08100	80.77259126
B	46.29927	80.4670722
C	39.52986	78.67773497
H	28.52601	80.08168118
X	46.17997	81.40069085

According to Table 4.1, result shown that the degree of crystallinity and crystallite size of all samples are highly similar, except sample C and H which have lower crystalline size compared to others with size of $39.52986nm$ and $28.52601nm$ respectively.

4.3 Vickers Hardness Testing

Table 4.2. shows the experimental result for Vickers hardness testing. Based on the result shown below that among the homogenized sample A, B, C, and H that sample H had significant lower hardness in comparison to else sample, thereby proven that the hardness of sample is not affected by the homogenization process parameters but the cooling rate of sample after homogenization process. According to Sun et al. (2014) research, the higher the cooling rate, the harder the sample. Therefore, sample H exhibited lower hardness in comparison to sample A, B and C as sample H is air-cooled, whereas sample A, B and C are forced air-cooled (Tam, 2019).

Table 4.2: Vickers hardness of the samples (Tam, 2019)

Sample	Vickers Hardness (HV)
A	56.6
B	60.9
C	61.4
H	38.3
X	54.3

4.4 Tensile & Compression Testing

Figure 4.2 and Figure 4.3 illustrate the experimental data for tensile and compression testing. Table 4.3 shows the tabulation form of sample's mechanical properties tested by tensile machine. Results shown that there is major difference in mechanical properties for homogenized samples and as-cast sample.
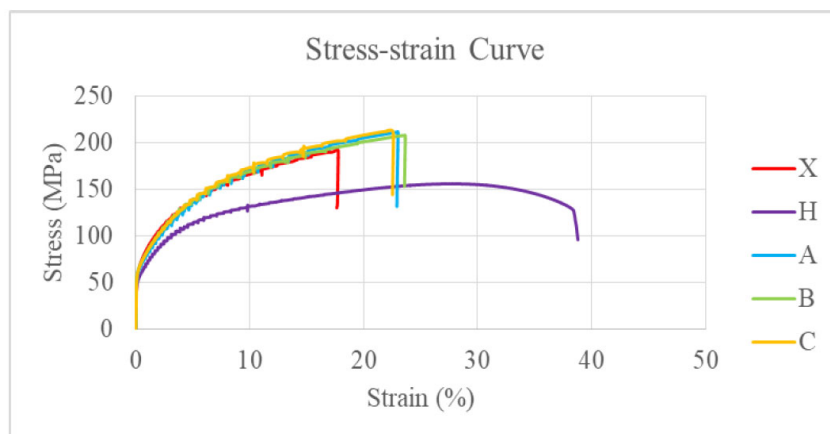
Figure 4.2: Tensile Stress-Strain Curve (Tam, 2019)

Table 4.3: Sample's Mechanical Properties (Tam, 2019)

Sample	Young's Modulus (GPa)	Yield Strength (MPa)	Ultimate Tensile Strength (MPa)	Percentage Elongation (%)
X	38.1	64.1	193.3	17.6
H	55.0	52.4	156.6	38.8
A	88.4	65.2	207.9	22.9
B	85.7	66.4	213.4	23.6
C	83.7	67.5	220.6	22.5

Figure 4.3: Compressive Stress-Strain Curve (Tam, 2019)

Tensile test result had validate the statement mentioned in Kelesoglu (2010) research. Kelesoglu (2010) research shown similar phenomenon as the sample subjected to higher temperature and time of homogenization increase, the elongation of samples rises. Tensile test result shown that among the samples that as-cast sample

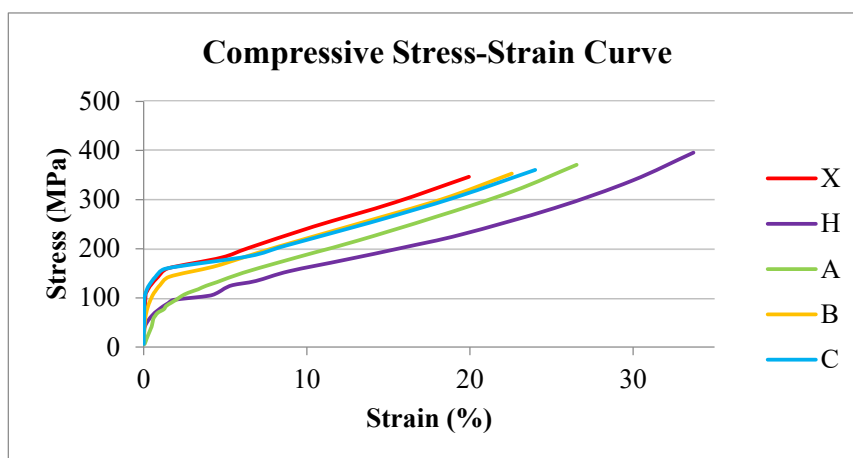X has the lowest strain percentage of 17.6%, whereas sample H has the highest strain percentage of 38.8%. This experimental outcome proven that homogenized samples does exhibited better ductility in comparison with as-cast sample that mentioned by Kumar, Grant and O'Reilly (2016) and Tang and Sritharan (1998).

However, tensile test result for sample A, B and C that homogenized under difference homogenization temperature and period did not exhibit major difference in elongation with a percentage of 22.9%, 23.6% and 22.5% respectively. This result does not tally with the experimental result shown in Kelesoglu (2010), whereby samples that subjected to higher homogenization temperature or long homogenization period had an increase in elongation percentage. This difference could be caused by the inappropriate laboratory preparation, as sample H which prepared by factory exhibited better ductility and lower stress in comparison to sample C that prepared in laboratory with similar homogenization process parameters.

Furthermore, compression test result also shown that in overall homogenized samples have better strain rate and lower stress compared to as-cast sample X, by which homogenized sample H has the highest strain rate and lowest stress among the samples.

4.5   Quantification of secondary phases

Table 4.4 illustrates the relative volume percentage of $\alpha - AlFeSi$ identified from samples that indicated using equation 2.1 based on $AlFeSi$ dispersoids identified from 20x-OM and 550x-SEM images.

Table 4.4: Relative volume percentage of α-AlFeSi ($\mathbf{f_\alpha}$) identified from OM and SEM images

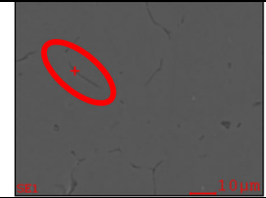| Sample	OM	SEM
	f_α (%)	f_α (%)
A	55.99118	43.97556
B	63.92636	53.43551
C	63.26828	52.69427
H	69.98845	67.76071
X	47.10459	48.75650

Based on Table 4.4, sample H has the highest degree of $\beta \rightarrow \alpha - AlFeSi$ transformation identified from OM or SEM images compared to others sample, whereas sample X has the lowest degree of transformation in compared to others sample based on OM images. In general, the degree of $\beta \rightarrow \alpha - AlFeSi$ transformation analysed from the images tally with experimental result mentioned by Kuijpers et al. (2003) and Kelesoglu (2010), whereby as-cast sample has the lowest relative percentage of $\alpha - AlFeSi$ while homogenized sample that experienced highest homogenization temperature or period has highest relative percentage of $\alpha - AlFeSi$ in compared to others homogenized sample.

Moreover, sample B and C had identified similar relative percentage of $\alpha - AlFeSi$ for OM and SEM images, whereby implying whether the increase in homogenization temperature or homogenization period both are viable options to improve the relative volume percentage of $\alpha - AlFeSi$ consist within sample.

Furthermore, the inconsistency of relative volume percentage of $\alpha - AlFeSi$ obtained from SEM images revealed the importance of sampling size. Based on Tam (2019) provided 20x-OM and 550x-SEM images shown that SEM images samples is taken under a higher magnification in comparison to OM images. Higher magnification causing smaller sample size taken by SEM images may led to low statistical power and inflated false discovery rate compared to OM images. This issue can be observed as according to relative volume percentage of $\alpha - AlFeSi$ identified from sample A is relatively lower than sample X, which does not tally with Kelesoglu (2010) as sample A is homogenized sample, whereas sample X is as-cast sample. Therefore, such phenomenon could be result from the small sampling size taken via SEM.

Table 4.5 shows the elemental composition of secondary phases which Tam (2019) identified as α and $\beta - AlFeSi$ via EDX point analysis.

Table 4.5: Atomic percentage of secondary phases analysed by EDX.

Secondary Phase	Atomic Percentage (%)			Atomic Ratio (R)
	Al	Fe	Si	$Fe:Si$
$\beta - AlFeSi$	95.34	1.36	1.43	0.951
$\alpha - AlFeSi$	94.97	1.88	1.12	1.679

Based on Table 4.5, the change in elemental composition was verified as $\beta \rightarrow \alpha - AlFeSi$ transformed. Result shown secondary phase appears to be morphology of $\beta - AlFeSi$ stated as Tang and Sritharan (1998) has $Fe:Si$ atomic ratio of 0.951, whereby falls within $\beta - AlFeSi$ elemental characterization parameter of $R \leq 1.5$. Furthermore, secondary phase which appears to be $\alpha - AlFeSi$ morphology as Kelesoglu (2010) mentioned has $Fe:Si$ atomic ratio of 1.679 that agreed with $\alpha - AlFeSi$ elemental characterization parameter of $R > 1.5$. Therefore, the EDX results were tally with Sweet et al. (2011) research study, whereby $Fe:Si$ atomic ratio for $AlFeSi$ dispersoid increases as $\beta - AlFeSi$ transform into $\alpha - AlFeSi$.

Figure 4.4 shows the size distribution of $MgSi$ precipitates of all sample which identified from 50x-OM images.
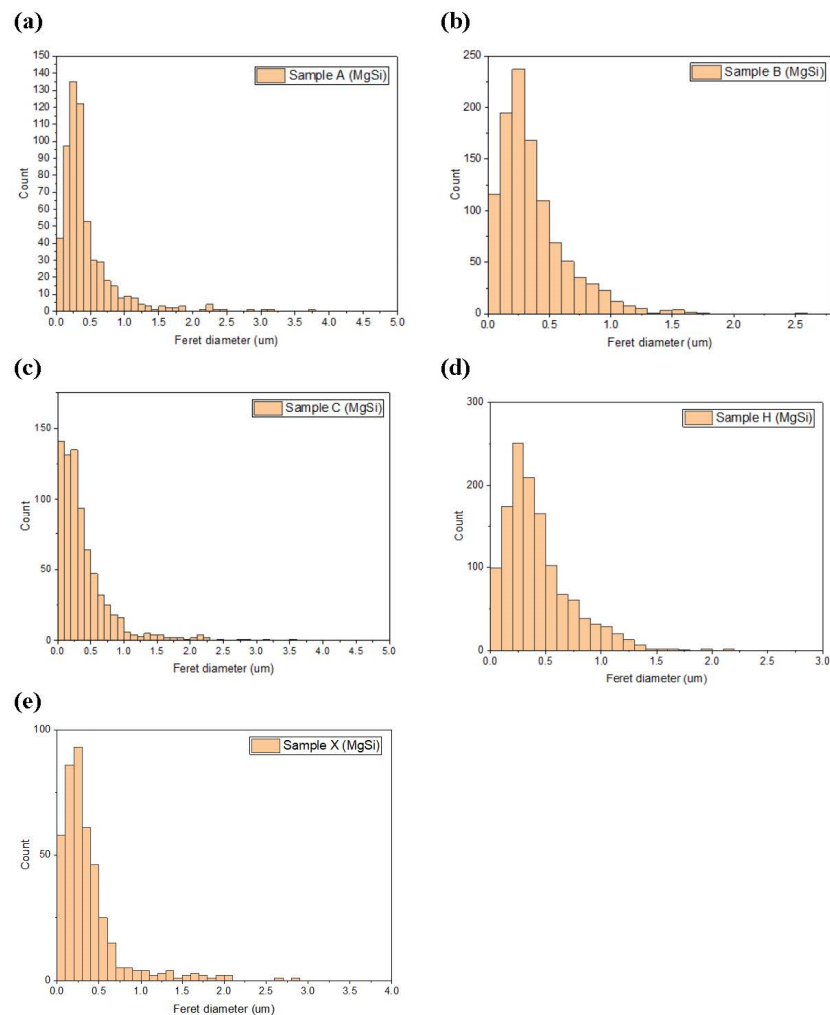
Figure 4.4: Size distribution of MgSi precipitates (a) Sample A, 2 hours lab homogenized at 540°C (b) Sample B, 6 hours lab homogenized at 560°C (c)Sample C, 3.5 hours lab homogenized at 540°C (d) Sample H, 3.5 hours factory homogenized at 540°C (e) Sample X, as-cast

Based on Figure 4.4, the overall number of $MgSi$ precipitates in sample X is significantly lesser than others sample, whereas sample H consist of highest count for $MgSi$ precipitates present within it. In addition, the overall size distribution patterns for all sample does not varies much, whereby based on data illustrated shown that all samples have mode of $0.25um$ for $MgSi$ precipitates ferret diameter. However, this phenomenon is differed from Sun et al. (2014) findings, whereby the size of $MgSi$ precipitates decrease as the cooling rate decreases, which according to Tam (2019) that

homogenized sample H experienced higher cooling rates than else homogenized samples.

Figure 4.5 shows the types of $MgSi$ precipitates discovered in all sample that categorized based on the defined optical characterization parameters for $MgSi$ precipitates. The precipitates were identified from 50x-OM images retrieved from Tam (2019) and processed in accordance to image processing techniques stated in methodology.
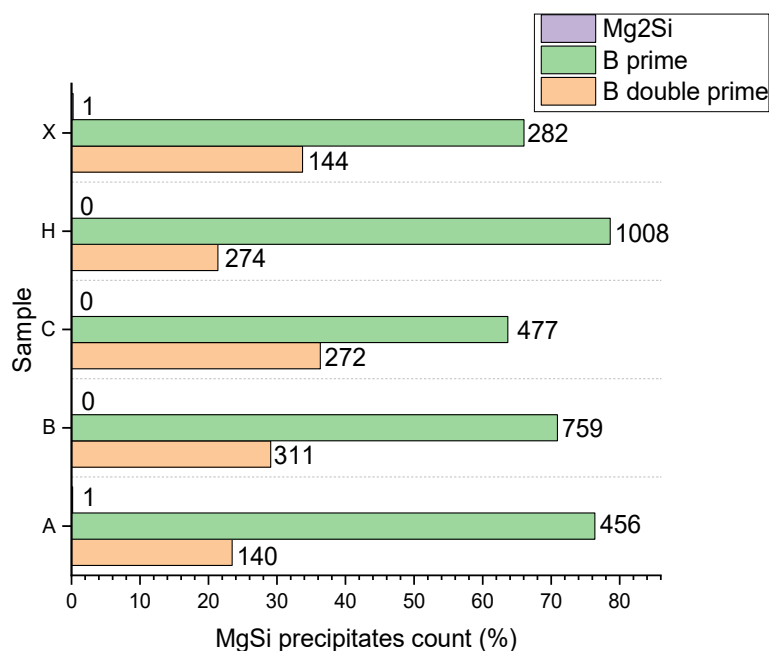

Figure 4.5: Types of MgSi precipitates

Based on Figure 4.5, the majority of $MgSi$ precipitates discovered in all sample via OM are $\beta'(Mg_{1.8}Si)$, follow by $\beta''(Mg_5Si_6)$ and lastly $\beta(Mg_2Si)$, whereby shown that there was no significant variance in the types of $MgSi$ precipitates under different homogenization parameter. However, the count of $MgSi$ precipitates discovered in each sample differ much, with factory homogenized sample H that consist of highest number of precipitates among others, whereas as-cast sample X has lowest number of precipitates. Referring to Mrówka-Nowotnik (2010) and Bowden (1984) that alloy's hardness is affected by the $Mg + Si$ dissolution within aluminium matrix. Higher number of $MgSi$ precipitates observed from homogenized sample H in comparison to as-cast sample X implied that hardness values for sample H shall be

lower that sample X. Based on the hardness test result, sample H is found to be 38.3HV which lower that sample X hardness value of 54.3HV, but contradictorily the hardness test result for sample A, B and C exhibit higher hardness compared to sample X even though the number of precipitates is higher. Therefore, an alternative parameter to correlate the relationship between $MgSi$ precipitates and alloy's hardness was illustrated in Figure 4.6. Figure 4.6 shows the total area of $MgSi$ precipitates of all sample identified from 50x-OM images.
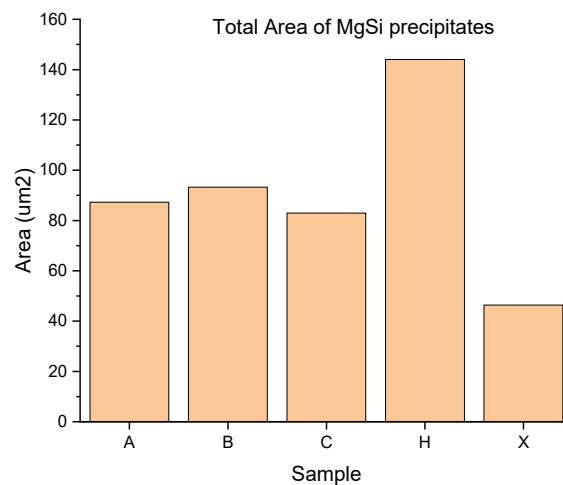

Figure 4.6: Total Area of MgSi precipitates

Based on Figure 4.6, the total area of $MgSi$ precipitates in sample H is significantly higher than others sample, whereas sample X consist of lowest area for $MgSi$ precipitates present within it. Consequently, no explanation could be made of the correlation between $MgSi$ precipitates and alloy's hardness since both parameters could not explain the contradictory result obtained. Instead, this phenomenon could be justified by the cooling rates subjected by samples according to Sun et al. (2014). In this paper, as-cast sample X was subjected to water quench, whereas homogenized samples A, B and C were subjected to air cooled and lastly homogenized sample H was subjected to forced-air cooled. Referring to the cooling rates subjected by samples, data shown that samples subjected to higher cooling rate have lesser total area of $MgSi$ precipitates and vice versa.

4.6 **Correlation between elongation percentage and relative percentage of α-AlFeSi**

Figure 4.7 shows overall the relationship between percentage of $\alpha - AlFeSi$ identified and elongation percentage of sample are linearly proportional to each other. The result is in good agreement with Kelesoglu (2010), which stated that homogenized alloy is more easily deformed as more α-AlFeSi phases consist within it since the phases are shorter and relatively rounder. This proven the feasibility of various techniques implemented by various researchers to evaluate the alloy's homogeneity through quantifying the degree of $\beta \to \alpha - AlFeSi$ phase transformation. Results implied that well-homogenized billet exhibited better ductility as higher the degree of $\beta \to \alpha - AlFeSi$ phase transformation occurs, thereby enhance the billet extrudability and end product surface quality. In addition, based on the degree of correlation between the quantified $AlFeSi$ dispersoids within sample and sample's ductility that OM is proven to be a more preferable material characterization techniques in comparison to SEM that falsely discovery the degree of $\beta \to \alpha - AlFeSi$ phase transformation for sample A. This issue had addressed in Chapter 4.5.
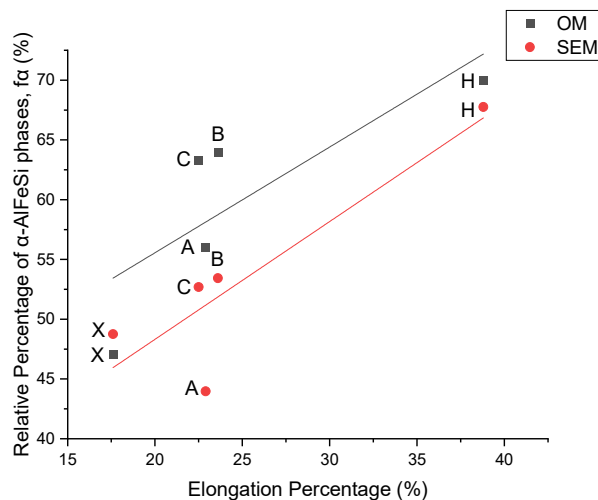

Figure 4.7: The relative ratio of α-AlFeSi phases in the samples shown as a function of elongation percentage.

4.7   Correlation between hardness and total area of MgSi precipitates

Figure 4.8 illustrates the relationship between the sample hardness and the total area of $MgSi$ precipitates identified from sample via scatter diagram.
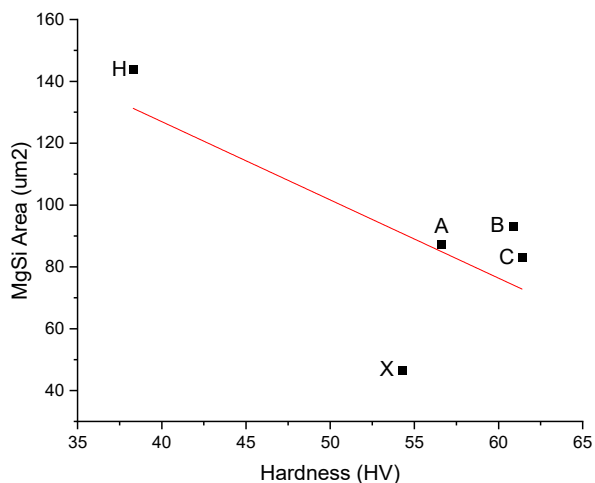

Figure 4.8: The total area of MgSi precipitates within sample shown as a function of sample hardness.

Figure 4.8 shows that there is clear relationship between sample hardness and total area of $MgSi$ precipitates. The higher the hardness, the lower the total area of $MgSi$ precipitates. However, this only work for homogenized sample. Sample X exhibited higher hardness than sample A, B and C even though the total area of $MgSi$ precipitates is lower. The possible reason may due to lower degree of $\beta \rightarrow \alpha - AlFeSi$ phase transformation in sample X as according to Triantafyllidis et al. (2015) the transformation will increase the level of Si content in solid solution. The increased level of Si content in sample A, B and C and relatively lower $MgSi$ precipitates could result increase in hardness values due to solid solution strengthening effect by higher Si content in solid solution, which causing greater hardness compared to as-cast sample X (Sun et al., 2014). Based on these findings, this technique to quantify $MgSi$ precipitate is proven to be feasible for evaluating the alloy's homogeneity as the changes in sample hardness is in good agreement with the total area of $MgSi$ precipitates.

4.8   Correlation between hardness and crystallite size

Figure 4.9 illustrates the relationship between the sample hardness and the calculated crystallite size via scatter diagram.
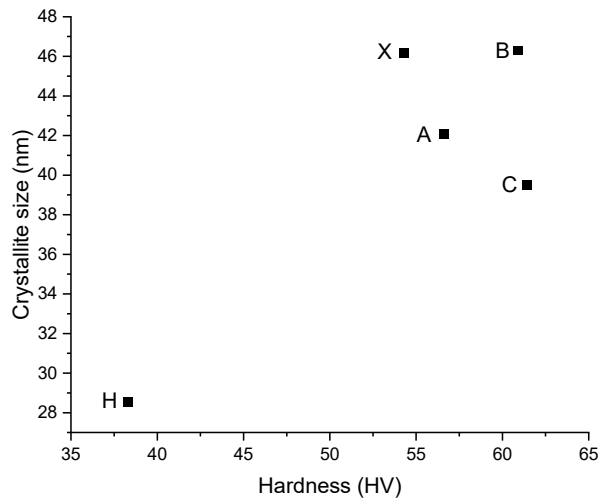

Figure 4.9: The crystallite size shows as a function of sample hardness.

Figure 4.9 shows that there is no relationship between sample hardness and crystallite size. According to Hall-Petch relationship that decrease in crystallite size resulting in increases of hardness values, which also been proven by Taha and Hammad (1990) that investigate the Hall-Petch relation for Al, Cu, Al-Cu alloy, and Al-MD 105. However, finding shown that sample H with smallest crystallite size has lowest hardness values with no clear correlation found between sample hardness and crystallite size, thereby proven in this research that the effect of crystallite size on sample hardness is negligible.

4.9   Correlation between hardness and crystallinity

Figure 4.10 illustrates the relationship between the sample hardness and crystallinity via scatter diagram.
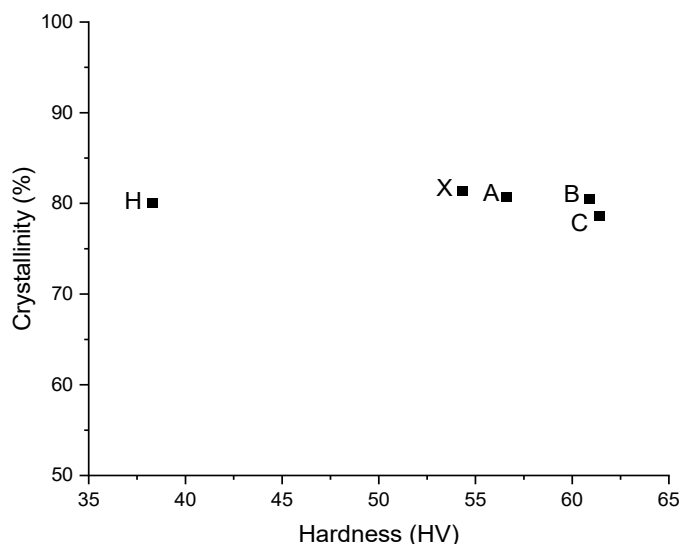
Figure 4.10: The crystallinity shows as a function of sample hardness.

Figure 4.10 shows that there is no relationship between sample hardness and degree of crystallinity. According to Arifutzzaman, Maleque and Sujan (2012) crystallization degree will greatly affect the hardness values. Authors indicated that the degree of crystallinity increases, the greater the hardness value. However, the high similarity of crystallization degree observed in all samples does not shown similar hardness as expected, whereby proven the effect of crystallization degree is negligible to sample hardness since no clear relationship was found between the change in hardness and sample's crystallinity.

4.10   Summary

In summary, various techniques implemented by researchers for quantifying secondary phase within alloy were proven to be feasible to evaluate alloy's homogeneity as this research found that the degree of $\beta \rightarrow \alpha - AlFeSi$ phase transformation shows in good agreement with the elongation percentage of sample, whilst the total area of $MgSi$ precipitate shows good agreement with sample hardness.   Furthermore, the assessment and comparison on technique to quantify secondary phases showed that implementing OM as material characterization technique is better option in comparison with technique that employ SEM. Microstructural images taken via OM

can detect $MgSi$ precipitates and provide larger sampling size in comparison to technique which employ SEM.

Lastly, this project found that only secondary phases with sample's mechanical properties, whereas else sample's microstructural properties such crystallite size and degree of crystallinity does not exhibit good correlation with sample's mechanical properties.

CHAPTER 5

CONCLUSIONS AND RECOMMENDATIONS

5.1 Conclusions

This research is to characterize and quantify the secondary phases present in 6063 aluminium alloy using an appropriate technique, thereby evaluate alloy's homogeneity. Secondary phases present within alloy namely, $AlFeSi$ dispersoid and $MgSi$ precipitates were quantitatively analysed through morphology discrimination based on microstructural images taken from OM and SEM or the difference in phase's chemical composition detected by EDX. Furthermore, this research also correlates the changes in alloy's mechanical properties with the secondary phases quantified via various material characterization techniques for assessing various techniques to evaluate alloy's homogeneity. Throughout the study, the following conclusion can be drawn:

I. 6063 aluminium alloy in general consist of two types of $AlFeSi$ dispersoid: $\beta - AlFeSi$ [needle-like] and $\propto -AlFeSi$ [as-cast: Chinese-script; homogenized: spheroidal]. As-cast alloy consist of lower relative percentage of $\propto -AlFeSi$ (Sample X: 47.1%), whereas well-homogenized alloy consists of high relative percentage of $\alpha - AlFeSi$ (Sample H: 69.9%) [higher soaking temperature or longer soaking period].

II. Ductility of homogenized alloy exhibit good correlation with the relative percentage of $\alpha - AlFeSi$ in microstructure. The higher the relative percentage of $\alpha - AlFeSi$, the higher the elongation percentage of alloy.

III. 6063 aluminium alloy in general consist of three types of $MgSi$ precipitates: $\beta'' (Mg_5Si_6)$ [smallest needle-like], $\beta' (Mg_{1.8}Si)$ [rod-like] & $\beta (Mg_2Si)$ [largest cube-like]. Precipitation of $MgSi$ precipitates is affected by cooling rate after the homogenization. Air-cooled sample H consist of greatest area of $MgSi$ precipitates identified, whereas water quenched sample X consist of lowest area.

IV. Hardness of homogenized alloy exhibit good correlation with the area of $MgSi$ precipitates in microstructure. The higher the hardness values, the lower the amount of $MgSi$ precipitates.

V. Elemental analysis via SEM with EDX is proven feasible to differentiate $AlFeSi$ dispersoids.

VI. Crystallinity and crystallinities size does not affect alloy's hardness.

5.2 Recommendations for future work

Based on the challenges faced and discussion made in this research study upon the quantification of secondary phase to evaluate alloy's homogeneity, several recommendations for future study on this topic are proposed. Recommendations proposed are:

I. Increase the sampling size. In this study only limited data is retrieved from senior's research work due to the unprecedented times of covid-19 resulting in some of the findings discovered by this study suffers low statistical power.

II. Discover the possibility of quantifying secondary phases via XRD. According to various researchers that XRD is proven to be one of the feasible characterization techniques to detect secondary phases present in Al-Mg-Si alloy (Hosseinifar and Malakhov, 2011; Kumar, Grant and O'Reilly, 2016; Kuijpers, 2014; Kuijpers et al., 2002, 2003). Although in this study, XRD analysis could not reveal the existence of secondary phases.

III. Increase homogenized sample alloys subjected to different cooling rates. In this study, homogenized alloys only subjected to forced air-cooled and air-cooled unlike the experiment conducted by Sun et al. (2014), which consist of three major different cooling rate: furnace cooled, air cooled, and water quenched. Addition of sample subjected to different cooling rate could enable deeper discovery on cooling rate effect to the precipitation of $MgSi$ precipitates.

REFERENCES

Anon 1997. *Basic Metallurgy : 6000 Series Extrusion Alloys*. Comalco Publication.

Arifutzzaman, A., Maleque, M.A. and Sujan, D., 2012. The Crystallinity and Hardness Properties of Al-Cu/SiCp New Composite Materials. *Advanced Materials Research*, [online] 576, pp.450–453. Available at: <https://www.scientific.net/AMR.576.450> [Accessed 29 Aug. 2021].

Asghar, G., Peng, L., Fu, P., Yuan, L. and Liu, Y., 2020. Role of Mg2Si precipitates size in determining the ductility of A357 cast alloy. *Materials and Design*, [online] 186, p.108280. Available at: <https://doi.org/10.1016/j.matdes.2019.108280>.

Belov, N.., Eskin, D.G. and Aksenov, A.A., 2005. Alloys of the Al-Mg-Si-Fe System. *Multicomponent Phase Diagrams: Applications for Commercial Aluminum Alloys*, pp.46–52.

Bowden, D.M., 1984. Third International Aluminum Extrusion Technology Seminar. *JOM: Journal of The Minerals, Metals & Materials Society*, 36(12), pp.25–28.

Cobden, R. and Banbury, A., 1994. Aluminium: Physical Properties, Characteristics and Alloys. *Talal*, [online] p.60. Available at: <http://www.alueurope.eu/talat/lectures/1501.pdf>.

Davis, J.R., 2001. *Alloying Understand The Basic*.

He, Y., Jia, Z., Sanders, R.E., Liu, Y., Ding, L., Xing, Y. and Liu, Q., 2017. Quantitative study of dissolution of Mg2Si during solution treatment in AA6014 alloy. *Journal of Alloys and Compounds*, [online] 703, pp.272–279. Available at: <http://dx.doi.org/10.1016/j.jallcom.2017.01.336>.

Hosseinifar, M. and Malakhov, D. V., 2011. The sequence of intermetallics formation during the solidification of an Al-Mg-Si alloy containing la. *Metallurgical and Materials Transactions A: Physical Metallurgy and Materials Science*, 42(3), pp.825–833.

Isadare, D., Adeoye, M., Adetunji, A., Oluwasegun, K. and Akinluwade, K., 2015. The Influence of Homogenization Treatment on Aging Response of 6063 Aluminium Alloy. *Advances in Research*, 5(3), pp.1–11.

Kelesoglu, E., 2010. A Study on Quantification of Homogenizing Treatment for Al-Mg-Si Alloy AA 6063. *Materialpruefung/Materials Testing*, 52(3), pp.156–159.

Kuijpers, N.C.W., 2014. *Kinetics of the β -AlFeSi to α -Al(FeMn)Si transformation in Al-Mg-Si alloys*.

Kuijpers, N.C.W., Kool, W.H., Koenis, P.T.G., Nilsen, K.E., Todd, I. and Van der Zwaag, S., 2002. Assessment of different techniques for quantification of α-Al(FeMn)Si and β-AlFeSi intermetallics in AA 6xxx alloys. *Materials Characterization*, 49(5), pp.409–420.

Kuijpers, N.C.W., Vermolen, F.J., Vuik, K. and Van Der Zwaag, S., 2003. A model of the β-AlFeSi to α-Al(FeMn)Si transformation in Al-Mg-Si alloys. *Materials Transactions*, 44(7), pp.1448–1456.

Kumar, S., Grant, P.S. and O'Reilly, K.A.Q., 2016. Evolution of Fe Bearing Intermetallics During DC Casting and Homogenization of an Al-Mg-Si Al Alloy. *Metallurgical and Materials Transactions A: Physical Metallurgy and Materials Science*, 47(6), pp.3000–3014.

Mrówka-Nowotnik, G., 2010. Influence of chemical composition variation and heat treatment on microstructure and mechanical properties of 6xxx alloys. *Archives of Materials Science and Engineering*, 46(2), pp.98–107.

Mukhopadhyay, P., 2012. Alloy Designation, Processing, and Use of AA6XXX Series Aluminium Alloys. *ISRN Metallurgy*, 2012(Table 1), pp.1–15.

Phongphisutthinan, C., Tezuka, H., Kobayashi, E. and Sato, T., 2013. Effects of β-Mg2Si precipitates on semi-solid microstructures of wrought AlMgSi based alloys produced by deformation-semi- solid-forming process. *Materials Transactions*, 54(4), pp.609–617.

Reiso, O., 2004. Extrusion of AlMgSi alloys. *Materials Forum*, 28, pp.32–46.

Rinderer, B., 2011. The metallurgy of homogenisation. 693, pp.264–275.

Rosefort, M., Matthies, C., Buck, H. and Koch, H., 2011. Using SEM and EDX for a Simple Differentiation of ?- and ?-AlFeSi-Phases in Wrought Aluminum Billets. *Light Metals 2011*, pp.711–716.

Røyset, J., Tundal, U., Espezel, C. and Reiso, O., 2019. Al-Mg-Si billets with high extrudability - State of the art and beyond. *Materials Today: Proceedings*, [online] 10, pp.185–192. Available at: <https://doi.org/10.1016/j.matpr.2018.10.395>.

Sarafoglou, P.I., Aristeidakis, J.S., Tzini, M.I.T. and Haidemenopoulos, G.N., 2016. Metallographic index-based quantification of the homogenization state in Extrudable Aluminum alloys. *Metals*, 6(5), pp.1–11.

Shafieizad, A.H., Zarei-Hanzaki, A., Abedi, H.R. and Al-Fadhalah, K.J., 2015. The Mg2Si phase evolution during thermomechanical processing of in-situ aluminum matrix macro-composite. *Materials Science and Engineering A*, [online] 644(August), pp.310–317. Available at: <http://dx.doi.org/10.1016/j.msea.2015.07.060>.

Sheppard, T., 1999. Processing of 6XXX alloys. In: *Extrusion of Aluminium Alloys*. [online] Springer US.pp.253–322. Available at:

<https://link.springer.com/chapter/10.1007/978-1-4757-3001-2_6> [Accessed 4 Mar. 2021].

Sun, Y., Johnson, D.R., Trumble, K.P., Priya, P. and Krane, M.J.M., 2014. Effect of Mg2Si Phase on Extrusion of AA6005 Aluminum Alloy. *Light Metals 2014*, 9781118889(i), pp.429–433.

Sweet, L., Zhu, S.M., Gao, S.X., Taylor, J.A. and Easton, M.A., 2011. The effect of iron content on the iron-containing intermetallic phases in a cast 6060 aluminum alloy. *Metallurgical and Materials Transactions A: Physical Metallurgy and Materials Science*, 42(7), pp.1737–1749.

Taha, A.S. and Hammad, F.H., 1990. Application of the Hall-Petch Relation to Microhardness Measurements on Al, Cu, Al-MD 105, and Al-Cu Alloys. *physica status solidi (a)*, [online] 119(2), pp.455–462. Available at: <https://onlinelibrary.wiley.com/doi/full/10.1002/pssa.2211190207> [Accessed 3 Sep. 2021].

Tam, H.M., 2019. EFFECT OF HOMOGENIZATION TREATMENT ON THE 6063 ALUMINIUM ALLOY. (September).

Tang, S.K. and Sritharan, T., 1998. Morphology of β-AlFeSi intermetallic in Al-7Si alloy castings. *Materials Science and Technology*, 14(8), pp.738–742.
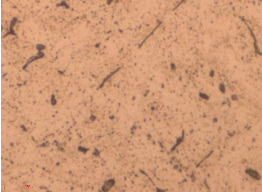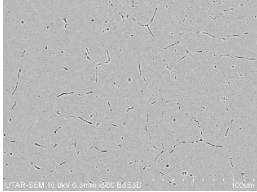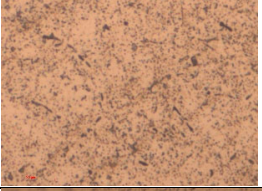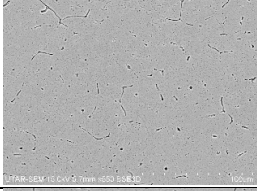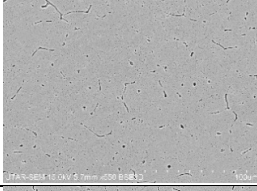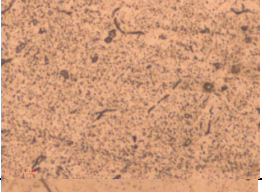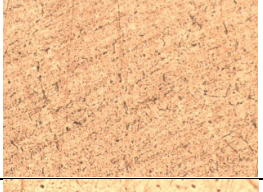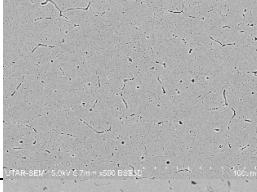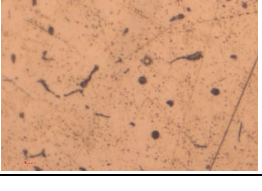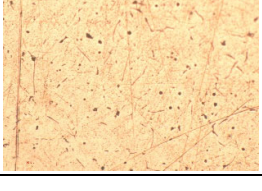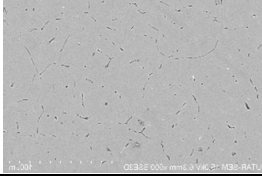
Triantafyllidis, G.K., Kiligaridis, I., Zagkliveris, D.I., Orfanou, I., Spyridopoulou, S., Mitoudi-Vagourdi, E. and Semertzidou, S., 2015. Characterization of the A6060 Al Alloy Mainly by Using the Micro-Hardness Vickers Test in Order to Optimize the Industrial Solutionizing Conditions of the As-Cast Billets. *Materials Sciences and Applications*, 06(01), pp.86–94.

Uttarasak, K., Chongchitnan, W., Matsuda, K., Chairuangsri, T., Kajornchaiyakul, J. and Banjongprasert, C., 2019. Evolution of Fe-containing intermetallic phases and abnormal grain growth in 6063 aluminum alloy during homogenization. *Results in Physics*, [online] 15(May), p.102535. Available at: <https://doi.org/10.1016/j.rinp.2019.102535>.

Vargel, C., 2004. The Most Common Wrought Aluminium Alloys. In: *Corrosion of Aluminium*. Elsevier.pp.61–69.

APPENDICES

APPENDIX A: OM and SEM images retrieved from Tam (2019) research work

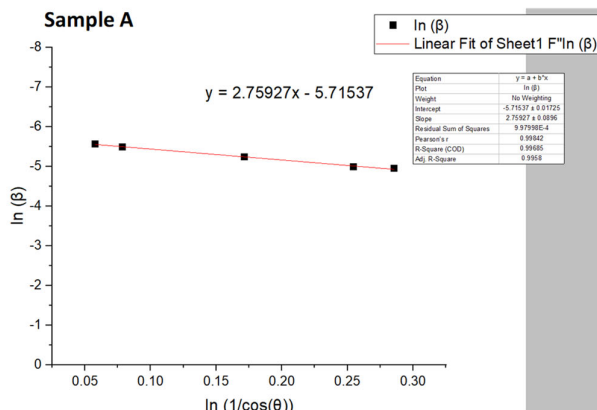| Sample	OM		SEM
	50x	20x	550x
A			
B			
C			
H			
X			

APPENDIX B: Scherrer equation and XRD deconvolution method

$$y - intercept = x = In\left(\frac{K\lambda}{D}\right)$$

$$e^x = e^{In\left(\frac{K\lambda}{D}\right)}$$

$$e^x = \frac{K\lambda}{D}$$

$$D = \frac{K\lambda}{e^x}$$

$$y - intercept = -5.71537$$

$$e^{-5.71537} = e^{In\left(\frac{K\lambda}{D}\right)}$$

$$D = \frac{K\lambda}{e^{-5.71537}} = \frac{(0.9 \times 0.15406nm)}{0.0032949} = 42.08100nm$$

APPENDIX B1: Sample calculation for sample A's average crystallite size via Scherrer equation

Sample A				Sample B		
	S.No				S.No	
	1	1286.7			1	1331.42
	2	504.72			2	634.62
	3	320.78			3	447.04
	4	514.18			4	515.38
	5	73.04			5	114
area of crystalline peaks		2699.42		area of crystalline peaks		3042.46
area of all peaks		3342		area of all peaks		3781
crytallinity		80.77259126		crytallinity		80.4670722
Sample C				Sample H		
	S.No				S.No	
	1	1187.46			1	2136.86
	2	535.96			2	372.26
	3	314.88			3	94.88
	4	367.82			4	183.4
	5	76.98			5	122.48
area of crystalline peaks		2483.1		area of crystalline peaks		2909.88
area of all peaks		3156.039		area of all peaks		3633.64
crytallinity		78.67773497		crytallinity		80.08168118
Sample X						
	S.No					
	1	1685.68				
	2	391.64				
	3	380.12				
	4	307.66				
	5	62.76				
area of crystalline peaks		2827.86				
area of all peaks		3474				
crytallinity		81.40069085				

APPENDIX B2: Sample calculation for all sample's crystallinity via XRD deconvolution method